

Modeling the Effects of Coordinated Multi-Beam Additive Manufacturing

Rachel Evans (✉ evans.382@wright.edu)

Wright State University College of Engineering and Computer Science

Joy Gockel

Wright State University College of Engineering and Computer Science

Research Article

Keywords: additive manufacturing, multi-beam laser powder bed fusion, thermal modeling

Posted Date: February 22nd, 2021

DOI: <https://doi.org/10.21203/rs.3.rs-172861/v1>

License: © ⓘ This work is licensed under a Creative Commons Attribution 4.0 International License.

[Read Full License](#)

Modeling the Effects of Coordinated Multi-Beam Additive Manufacturing

Rachel Evans^a and Joy Gockel^a

^a Wright State University, Department of Mechanical and Materials Engineering
3640 Colonel Glenn Hwy.
Dayton, OH 45435 USA

Corresponding Author: Rachel Evans; evans.382@wright.edu

Acknowledgements

This work was funded by an Ohio Space Grant Consortium Fellowship. The authors would like to thank Dr. Alex Plotkowski from Oak Ridge National Laboratory for valuable conversations and the development of the semi-analytical modeling code modified for this work.

Abstract

In additive manufacturing (AM), it is necessary to know the influence of processing parameters in order to have better control over the microstructure and mechanical performance of the part. Laser powder bed fusion (LPBF) AM is beneficial for many reasons; however, it is limited by the thermal solidification conditions achievable in the available processing parameter ranges for single-beam processing methods. Therefore, this work investigates the effect of multiple, coordinated heat sources, which are used to strategically modify the melting and solidifying in the AM process. To model this, existing thermal models of the LPBF process have been modified to include the effects of multiple, coordinated laser beams. These computational models are used to calculate melt pool dimensions and thermal conditions (thermal gradient and cooling rate). Furthermore, the results of the simulations are used to determine the influence of the distance between the coordinated laser beams in different configurations. The multi-beam scanning strategies modeled in the present study are shown to alter both melt pool shape and size, and the thermal conditions at the onset of solidification. However, these variations are not shown to result in alterations in the grain morphology of Ti-6Al-4V components. This predictive method used in this research provides insight into the effects of using multiple coordinated beams in LPBF, which is a necessary step in increasing the capabilities of the AM process.

Keywords: *additive manufacturing, multi-beam laser powder bed fusion, thermal modeling*

1 Introduction

The laser powder bed fusion (LPBF) additive manufacturing (AM) process allows for easy customization of parts with high resolution and small feature sizes. However, components that are made via LPBF often contain undesirable features such as residual stresses, surface defects, porosity, and microstructural inhomogeneities [1]. In most cases, the presence of these features drastically influences the mechanical performance of the part. Therefore, understanding the processing causes of these features will allow for better control of these features, which provides the potential to improve the overall quality and efficiency of the LPBF process. Microstructural inhomogeneities are an important concern in the LPBF process. These non-uniformities include a variety of microstructural aspects; however, this research is mainly concerned with variations in the grain size and morphology due to changes in the thermal behavior of the process. Variations in both grain size and morphology are known to have a strong influence on the mechanical performance of the final structure [2]. As a result, the thermal behavior of the LPBF process is important to understand in predicting the influence of the processing on the microstructure and ultimately the mechanical performance in the LPBF process.

In many cases, multi-beam LPBF processes are used to create parts in a parallel fashion, where multiple laser beams are used to independently create separate parts with increased productivity [3, 4]. However, little research has been conducted to investigate the effects of multi-beam LPBF with coordinated heat sources, which has the potential to offer better control of the thermal conditions, microstructure, and mechanical performance of the part. In the coordinated multi-beam LPBF process, multiple laser beams are used on the same scan field at a specified offset distance apart. As a result, the melt pool seen in coordinated multi-beam LPBF consists of two melted regions. The size and shape of this double melt pool is strongly influenced by the distance between the heat sources; as the lasers are spread further apart, the heated areas will have less of an influence on each other. Eventually, this will cause discrete melt pools with lengths and depths that approach the same results as a single laser beam. When the lasers are close together,

however, the melt pool looks similar to the one shown in Fig. 1, where the two melted regions overlap to form a single melt pool. Utilizing a coordinated multi-beam scanning strategy provides potential avenues for tailored thermal conditions, although not much research has been done for this type of scanning strategy because the experimental capability is not readily available. As a result, more research needs to be conducted to increase the understanding of the multi-beam LPBF process.

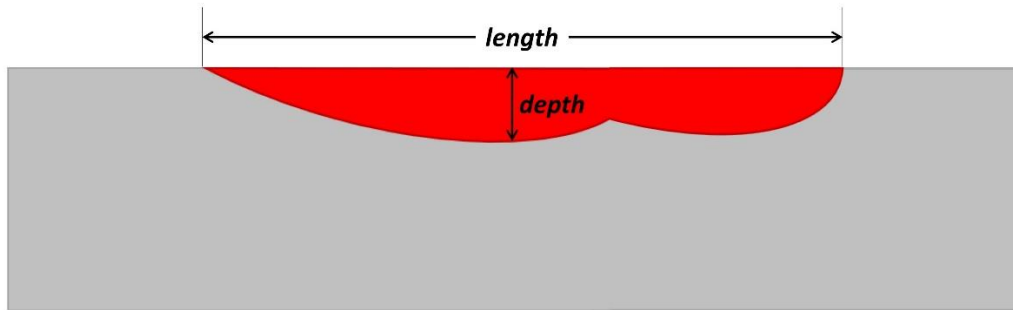


Fig. 1 Melt pool dimensions for multi-beam LPBF

Although there is not much existing research that studies coordinated multi-beam LPBF, few researchers have proved that the addition of a second laser beam has potential to improve different aspects of the LPBF process. For example, Heeling et al. used a computational modeling approach to investigate the effects of various coordinated multi-beam scan strategies. The resulting simulations show that the addition of a second laser beam, whether the offset is in-line or perpendicular to the scan direction, decreases both the thermal gradients and residual stresses in the part [5]. In another work by Heeling et al., a multi-beam LPBF process is used with a second, larger laser beam located at a specified offset distance in-line with the scan direction. In this case, the experiments show that multi-beam scan strategies result in smoother surfaces and more dense parts [6]. Abe et al. used a multi-beam system to create test specimens, which were shown to improve the ductility, residual stresses, hardness, and bending strength as compared to specimens manufactured with single-beam LPBF [7]. Aggarangsi et al. used a thermomechanical model to study the effects of using a localized preheating strategy in powder bed fusion of thin wall geometries. As a result, the preheating effects were shown to significantly influence the temperature distribution and thermal gradients, causing a decrease in residual stresses [8].

Overall, coordinated multi-beam LPBF has the capability to offer many advantages as opposed to single-beam LPBF. However, there is more research that needs to be done to explore the effects of adding a second, coordinated laser heat source. Because there is currently a lack of multi-beam LPBF machines commercially available, however, it is difficult to experimentally determine the effects of the coordinated multi-beam process. As a result, thermal modeling is used here to study the effects of a second heat source on the temperature distributions and thermal conditions throughout the build process. The purpose of this research is to determine the impact of utilizing a coordinated multi-beam configuration in LPBF. Moreover, this research aims to utilize computer simulations to predict the influences of a second heat source on both melt pool geometry and microstructure to guide future equipment development strategies.

2 Modeling Approaches

2.1 Multi-Beam Rosenthal Solution

The Rosenthal solution [9] is a 3-D solution to the heat equation for a point heat source traveling at a constant speed. This solution can be translated to multi-beam LPBF applications by superimposing the effects of multiple heat sources on the same scan field, as depicted in Fig. 2. A similar method has been used in the past to represent an insulated free edge [10]. In this configuration, however, two laser heat sources travel in the positive x -direction at speed V with absorbed laser power αQ . The system is modeled on the $y_0 = 0$ plane to obtain the solution that corresponds to the maximum melt pool depth.

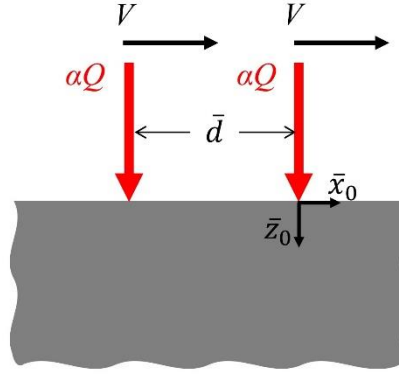


Fig. 2 The coordinated multi-beam LPBF configuration that is modeled by the Rosenthal solution

The multi-beam Rosenthal solution assumes steady state conditions, a semi-infinite domain, and constant and uniform material properties. The dimensionless form of the equation, given by Vasinota et al. [11], computes the non-dimensional temperature due to the heat source. This dimensionless form can be modified to include the effects of a second heat source to obtain Equation (1), which calculates the dimensionless temperature, \bar{T} , due to two heat sources:

$$\bar{T} = \frac{e^{-\left(\bar{x}_0 + \sqrt{\bar{x}_0^2 + \bar{z}_0^2}\right)}}{2\sqrt{\bar{x}_0^2 + \bar{z}_0^2}} + \frac{e^{-\left((\bar{x}_0 + \bar{d}) + \sqrt{(\bar{x}_0 + \bar{d})^2 + \bar{z}_0^2}\right)}}{2\sqrt{(\bar{x}_0 + \bar{d})^2 + \bar{z}_0^2}} \quad (1)$$

The dimensionless distance between heat sources, \bar{d} , and the dimensionless coordinates \bar{x}_0 , \bar{y}_0 , and \bar{z}_0 are defined in Equation (2):

$$\bar{d} = \frac{d}{2k/\rho c V}, \quad \bar{x}_0 = \frac{x_0}{2k/\rho c v}, \quad \bar{y}_0 = \frac{y_0}{2k/\rho c v}, \quad \text{and} \quad \bar{z}_0 = \frac{z_0}{2k/\rho c v} \quad (2)$$

The boundary of the melt pool is calculated by setting Equation (1) equal to the dimensionless melting temperature, \bar{T}_m , which can be found with Equation (3):

$$\bar{T}_m = \frac{T_m - T_0}{\left(\alpha Q / \pi k\right) \left(\rho c V / 2k\right)} \quad (3)$$

where T_m is the melting temperature, T_0 is the preheating temperature, α is the absorptivity of the laser heat source, Q is the laser power, k is the thermal conductivity, ρ is the material density, c is the specific heat, and V is the laser speed.

As discussed by Bontha et al. [12, 13], the solidification cooling rate and thermal gradient are found through differentiation of Equation (1). The dimensionless cooling rate $\partial\bar{T}/\partial\bar{t}$ can be calculated by taking the partial derivative of Equation (1) with respect to time. The dimensionless thermal gradient $|\nabla\bar{T}|$ is found by taking the magnitude of the x , y , and z components; however, the quantity $\partial\bar{T}/\partial\bar{y}_0$ is equal to zero on the $y_0 = 0$ plane. Therefore, the dimensionless thermal gradient, given by Equation (4), on the maximum melt pool plane becomes:

$$|\nabla\bar{T}| = \sqrt{\left(\frac{\partial\bar{T}}{\partial\bar{x}_0}\right)^2 + \left(\frac{\partial\bar{T}}{\partial\bar{z}_0}\right)^2} \quad (4)$$

where $\partial\bar{T}/\partial\bar{x}_0$ and $\partial\bar{T}/\partial\bar{z}_0$ are found by taking the appropriate partial derivatives of Equation (1).

It is important to note that the cooling rate and thermal gradient solutions approach the single-beam Rosenthal solution as d approaches infinity. Therefore, the simulations for multi-beam LPBF with $d = \infty$ can be modeled with the single-beam Rosenthal solution.

2.2 Multi-Beam Semi-Analytical Approach

In order to include time-dependent heat transfer effects, the LPBF process can be modeled with the semi-analytical approach [14]. This approach utilizes a transient heat conduction solution to compute temperature data as a result of a circular ring heat source [15, 16, 17, 18]. The semi-analytical model assumes a semi-infinite domain and neglects the effects of latent heat and heat loss due to vaporization and convection, while also assuming constant and uniform material properties. This approach has been used in previous studies to investigate quantities within LPBF such as melt pool size and shape, temperature distributions, and solidification thermal conditions [19, 20].

The effects of two heat sources can be superimposed to determine a solution for multi-beam LPBF. The coordinated multi-beam LPBF scan strategies that are modeled with the semi-analytical solution are shown in Fig. 3. In the first arrangement, two laser beams at a specified offset distance apart travel in the positive x -direction a constant speed. This configuration is very similar to the one modeled by the Rosenthal solution; however, the coordinate system is located differently. In the section laser arrangement, two lasers at independent laser powers travel in the positive x -direction at a constant speed. Finally, the last laser arrangement utilizes two identical lasers with an offset in the y -direction. A detailed list of the processing parameters used in this work is shown in Table 1.

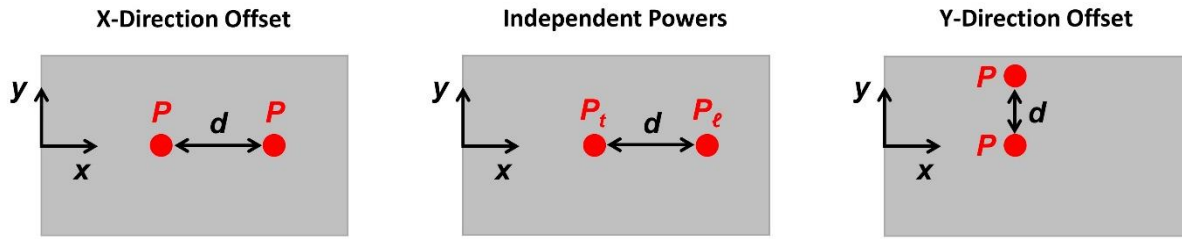


Fig. 3 The scanning strategies that are modeled by the multi-beam semi-analytical model

	Leading Laser Power (W)	Trailing Laser Power (W)	Speed (mm/s)	Laser Offset Distance
Identical beams with x-direction offset	300	300	750	0 mm
				0.25 mm
				0.5 mm
				1 mm
				2 mm
				∞
Independent powers with x-direction offset (Preheating)	100	300	750	0.25 mm
	150			
	200			
	250			
Independent powers with x-direction offset (Post-heating)	300	100	750	0.25 mm
		150		
		200		
		250		
Identical beams with y-direction offset	300	300	750	50 μm
				100 μm
				150 μm
				200 μm

Table 1 The laser processing parameters used in this work

The multi-beam semi-analytical solution, which uses the variables given in Table 2, has been obtained by superimposing the effects of two heat sources in the semi-analytical model. This solution is given by Equation (5):

$$\begin{aligned}
T(x, y, z) = T_0 + \frac{1}{c_p \rho (4\pi a)^{3/2}} \cdot \int_{\tau_i=0}^{\tau_i=t} \left[\frac{q_t}{\tau^{3/2}} \exp\left(-\frac{r_0^2 + x^2 + y^2 + z^2}{4a\tau}\right) \cdot I_0\left(\frac{r_0}{2a\tau} \sqrt{x^2 + y^2}\right) \right. \\
\left. + \frac{q_\ell}{\tau^{3/2}} \exp\left(-\frac{r_0^2 + (x + d_x)^2 + (y + d_y)^2 + z^2}{4a\tau}\right) \cdot I_0\left(\frac{r_0}{2a\tau} \sqrt{(x + d_x)^2 + (y + d_y)^2}\right) \right] d\tau_i
\end{aligned} \quad (5)$$

where the applied laser power, q , is defined as the product between the absorption coefficient α and the applied laser power P , given in Equation (6):

$$q = \alpha P \quad (6)$$

Variable	Description	Units
$T(x, y, z)$	Temperature at point (x, y, z)	K
T_0	Initial temperature	K
q_t	Absorbed power of trailing beam	J/s
q_ℓ	Absorbed power of leading beam	J/s
c_p	Specific heat	J/K
ρ	Material density	g/cm ³
a	Thermal diffusivity	m ² /s
τ_i	Integration time step	s
t	Time	s
τ	Time available for conduction	s
r_0	Radius of heat source	m
I_0	Bessel function of the first kind, zero order	none
d_x	Distance between laser beams (x -direction)	m
d_y	Distance between laser beams (y -direction)	m

Table 2 Variables used in the semi-analytical approach

Similar to the Rosenthal solution, the semi-analytical solution can be differentiated to obtain the cooling rates and thermal gradients. The cooling rate is found through partial differentiation of Equation (5) with respect to t . The thermal gradient is found through the following equation:

$$|\nabla T| = \sqrt{\left(\frac{\partial T}{\partial x}\right)^2 + \left(\frac{\partial T}{\partial y}\right)^2 + \left(\frac{\partial T}{\partial z}\right)^2} \quad (7)$$

where $\partial T/\partial x$, $\partial T/\partial y$, and $\partial T/\partial z$ are the partial derivatives of Equation (5) with respect to x , y , and z , respectively.

Just like the Rosenthal solution, the semi-analytical model approaches the single-beam solution as d approaches infinity. Therefore, the simulations for multi-beam LPBF with $d = \infty$ can be modeled with the single-beam semi-analytical solution.

3 Results and Discussion

3.1 Identical Beams with X-Direction Offset

The results in Fig. 4 show the melt pool geometries on the x - z plane for six different scan strategies as predicted by the Rosenthal solution. These simulations represent multi-beam scan strategies with offset distances of 0 mm, 0.25 mm, 0.5 mm, 1 mm, 2 mm, and ∞ . Here, the Rosenthal model predicts a single melt pool for all simulations with offset distances that are less than or equal to 1 mm; however, the simulation for 2 mm exhibits two discrete melt pools. In addition, an increase in d is shown to cause an increased melt pool length and a decreased melt pool depth.

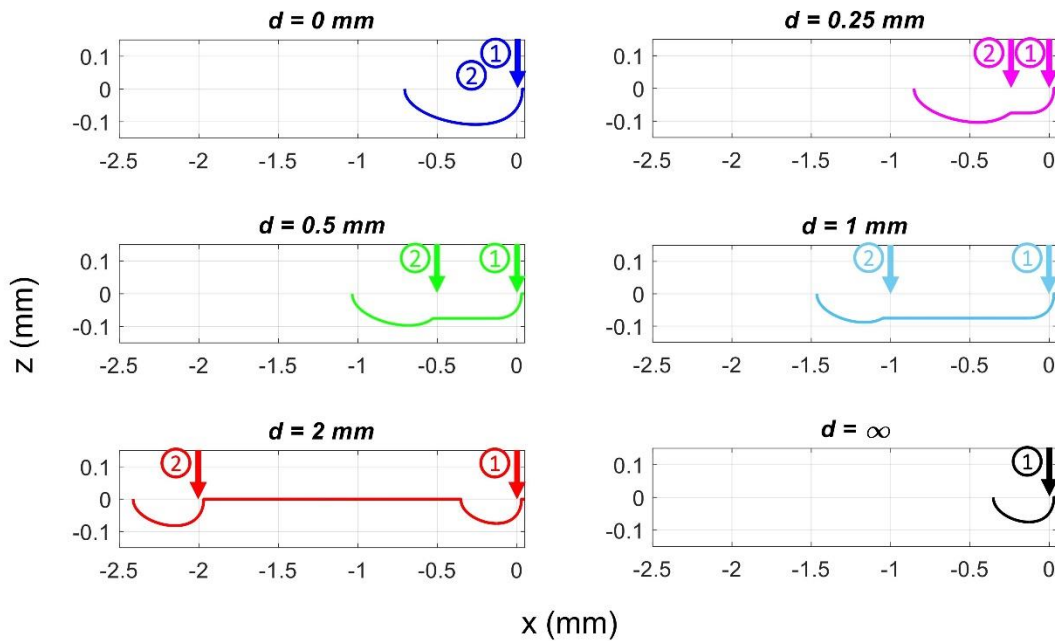


Fig. 4 Melt pool geometries of multi-beam LPBF, as predicted by the Rosenthal solution

The results in Fig. 5 show the melt pool geometries on the x - z plane for the same six scan strategies; however, these were calculated with the multi-beam semi-analytical model after a steady state had been reached. As expected, increasing d results in an increased melt pool length and a decreased melt pool depth. Additionally, the semi-analytical model predicts a single melt pool for offset distances of 0 and 0.25 mm; however, the remainder of the simulations predict two discrete melt pools.

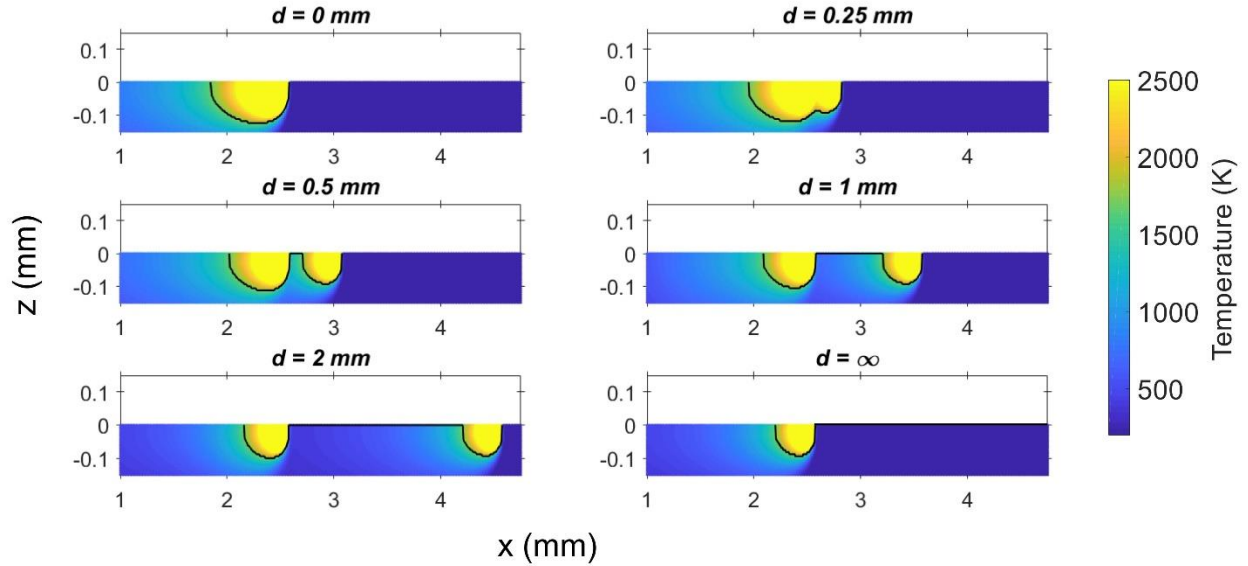


Fig. 5 Melt pool geometries of multi-beam LPBF, as predicted by the semi-analytical model

The maximum melt pool depths and lengths for both the Rosenthal and semi-analytical simulations are summarized in Table 3. It is important to note that the lengths are measured from the front of the leading melt pool to the end of the trailing melt pool in the cases that result in multiple, discrete melt pools. As expected, an increase in the distance between lasers generally causes a decrease in melt pool depth and an increase in melt pool length. This is because spreading out the lasers results in a longer melt pool that does not melt as far into the material. As this distance increases further, the affected region from each of the laser beams becomes less overlapped, and the melt pools split into two, discrete melt pools.

	<i>Rosenthal</i>		<i>Semi-Analytical</i>	
	Maximum Melt Pool Depth (μm)	Melt Pool Length (μm)	Maximum Melt Pool Depth (μm)	Melt Pool Length (μm)
$d = 0 \text{ mm}$	108.5	741.6	128.1	731.2
$d = 0.25 \text{ mm}$	103.9	882.1	121.9	878.1
$d = 0.5 \text{ mm}$	96.8	1065.4	115.6	1062.5
$d = 1 \text{ mm}$	88.3	1494.4	106.3	1490.6
$d = 2 \text{ mm}$	81.5	2443.4	100.0	2434.4
$d = \infty$	75.3	383.1	93.8	378.1

Table 3 The expected melt pool depths and lengths for multi-beam LPBF, as predicted by both the Rosenthal solution and the semi-analytical model

The next results show the thermal conditions for the same six simulations that were described above. For these results, both the cooling rate and thermal gradient were calculated at the boundary of the melt pool's trailing edge because this is the location at which the material begins to solidify. Fig. 6 shows the cooling rates versus the normalized melt pool depth, using both

the Rosenthal solution and the semi-analytical solution. As shown on the plots, an increase in distance results in an increase in the cooling rate, which also suggests a decrease in grain size. This trend was expected; spreading the beams farther apart causes the inputted heat to become less localized, thus increasing the rate at which the material cools down. Similarly, the thermal gradients were plotted against the normalized melt pool depth, which is shown in Fig. 7. Here, it is seen that the thermal gradient increases as the lasers are spread farther apart, although the results are very similar for $d = 0, 0.25$ mm, and 0.5 mm. This implies that the distance between lasers has a small influence the thermal gradient; however, this influence is negligible for small values of d .

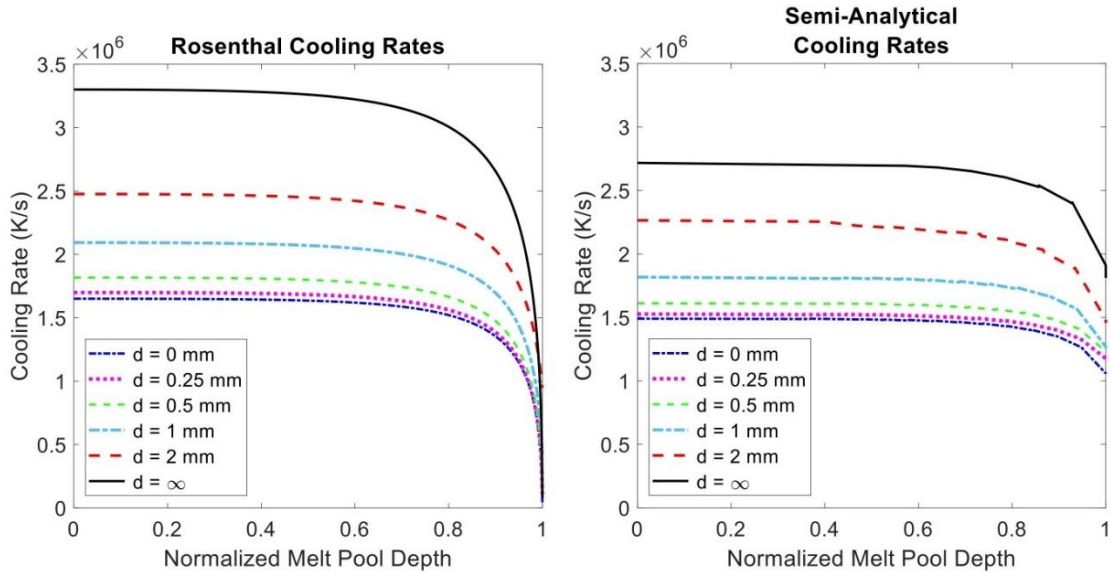


Fig. 6 Cooling rate vs. normalized melt pool depth in multi-beam LPBF with x-direction beam offset. These results were obtained with both the Rosenthal solution (left) and the semi-analytical solution (right)

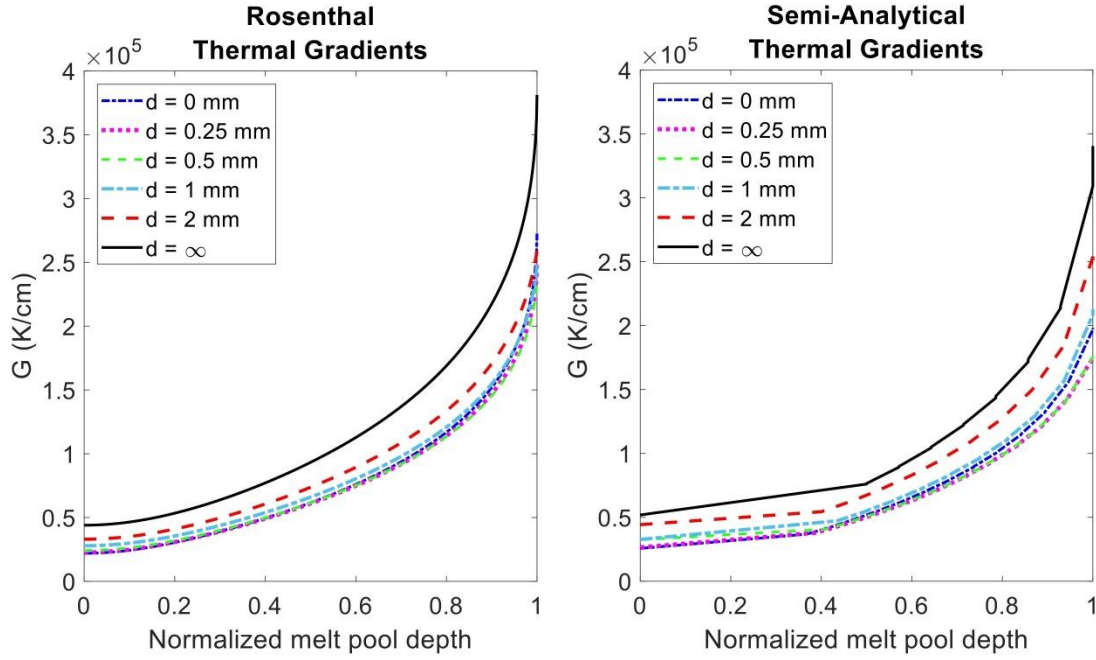


Fig. 7 Thermal gradient vs. normalized melt pool depth in multi-beam LPBF with x-direction beam offset. These results were obtained with both the Rosenthal solution (left) and the semi-analytical solution (right)

The cooling rates and thermal gradients were then used to create solidification maps in order to predict grain morphology. Columnar grains are elongated and anisotropic, while equiaxed grains are nearly equal in all directions. The solidification map plots the thermal gradient, G , versus the solidification rate, R , which is defined in Equation (8):

$$R = \frac{1}{G} \frac{\partial T}{\partial t} \quad (8)$$

The solidification maps, shown in Fig. 8, use the morphology regions determined by Kobryn et al. [10] for Ti-6Al-4V in AM processes. It can be observed that all the distances modeled here result in mixed grains that transition to columnar grains with increasing melt pool depth. This is true for both the Rosenthal solution and the semi-analytical model. The plots show that an increase in d causes the points to shift slightly above and to the right. This suggests that the distance between lasers has an effect on the G -vs- R results; however, the points remain in the same morphology regions regardless of the distance. As a result, the simulations indicate that the distance between lasers has a negligible influence on the grain morphology.

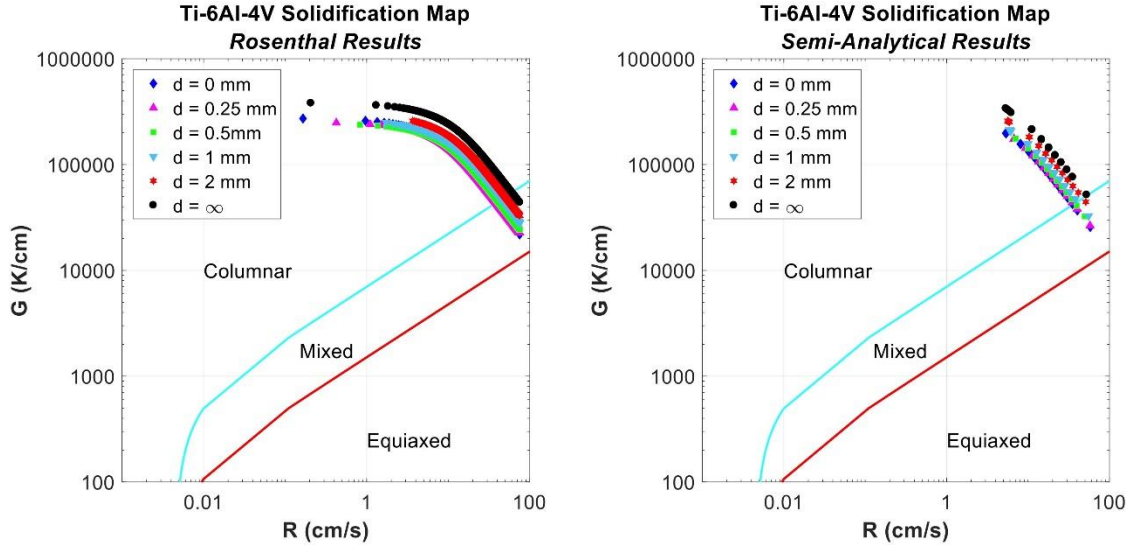


Fig. 8 Solidification maps for multi-beam LPBF, using both the Rosenthal (left) and semi-analytical (right) approaches

As compared to the results provided by the Rosenthal solution, the semi-analytical model consistently predicted melt pools with slightly shorter lengths and larger depths. Although, the general trends between melt pool size and laser offset distance remained the same for both approaches. One major difference between the two models, however, was that the Rosenthal model predicted single melt pools for laser offset distances of 0.5 mm and 1 mm, while the semi-analytical model predicted two discrete melt pools for simulations with the same parameters. These differences are likely due to the steady-state and the point heat source assumptions in the Rosenthal solution, whereas the semi-analytical model includes transient effects and models the heat source as a circular ring with a definable radius. However, despite these differences, both models predicted very similar thermal conditions, with slightly slower semi-analytical cooling rates and nearly equal thermal gradients provided by both approaches. Additionally, when plotting these thermal conditions on a solidification map, the results are very similar to one another.

3.2 Independent Powers with X-Direction Offset

The results in Fig. 9 correspond to simulations for both preheating and post-heating multi-beam LPBF processes. In the preheating simulations, the leading laser beam applies less power than the trailing laser beam. For each of these simulations, the power of the trailing laser beam is 300 W, and the power of the leading laser beam is varied. Conversely, the post-heating multi-beam LPBF simulations model the case where the trailing laser beam applies less power than the leading laser beam. In these simulations, the power of the leading laser beam remains constant at 300 W and the power of the trailing laser beam is varied. The absorption coefficient remains constant at 0.35 and the speed of each of the lasers is 750 mm/s for all simulations. The offset distance for each of the simulations is 0.25 mm, and the results were taken on the $y = 0$ plane after a steady-state condition was met. The maximum melt pool depths and lengths for these simulations are summarized in Table 4. As expected, both the melt pool length and depth increase as the power increases, for both the preheating and post-heating scanning strategies. However, these dimensions are slightly larger in the preheating simulations than in the post-heating simulations. Additionally,

all post-heating simulations resulted in a single melt pool, whereas the preheating simulations with low leading powers resulted in multiple, discrete melt pools.

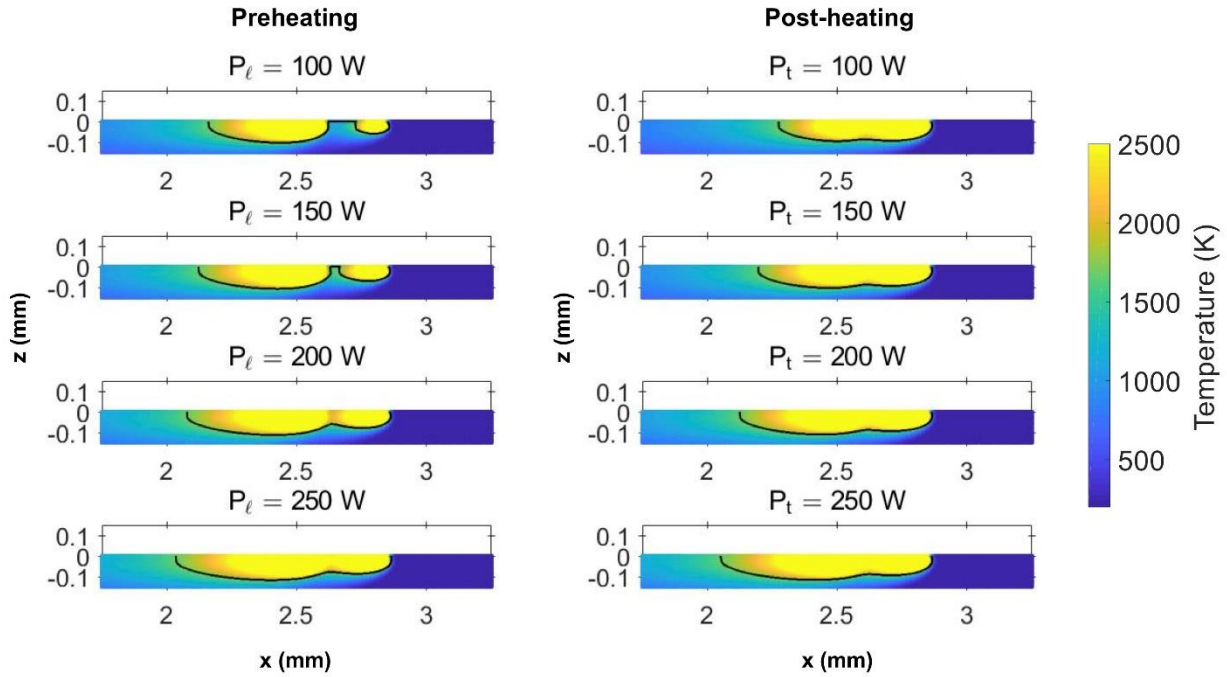


Fig. 9 Melt pool results for preheating and post-heating multi-beam LPBF

	<i>Preheating</i>		<i>Post-heating</i>	
	Maximum Melt Pool Depth (μm)	Melt Pool Length (μm)	Maximum Melt Pool Depth (μm)	Melt Pool Length (μm)
<i>P = 100 W</i>	103.1	696.9	96.9	590.6
<i>P = 150 W</i>	109.4	737.5	103.1	668.8
<i>P = 200 W</i>	112.5	784.4	109.4	740.6
<i>P = 250 W</i>	118.8	831.3	115.6	815.6

Table 4 Melt pool dimensions for both preheating and post-heating multi-beam LPBF scan strategies

The following images show the resulting thermal conditions for the eight simulations shown above. The cooling rates and thermal gradients here were calculated at the trailing edge of the melt pool boundary. Fig. 10 shows the cooling rates versus the normalized melt pool depth for both the preheating and post-heating simulations. As shown on the plot, an increase in power results in a decrease in the cooling rate for both preheating and post-heating. Additionally, the cooling rates for preheating processes are very close to the cooling rates provided by the post-heating processes. Next, the thermal gradients were plotted against the normalized melt pool depth, as shown in Fig. 11. As shown on the plot, an increase in power results in a decrease in the thermal

gradient, although the variations seen here are slight. Additionally, the thermal gradients provided by the preheating processes are very close to the thermal gradients produced by the post-heating scan strategies.

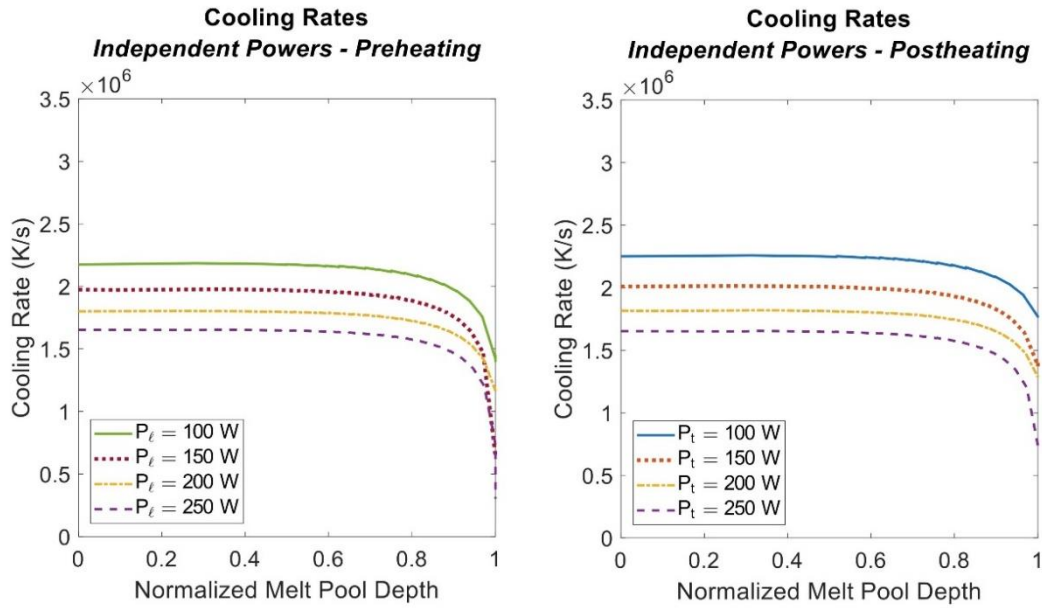


Fig. 10 Cooling rate vs. normalized melt pool depth for both preheating and post-heating multi-beam scan strategies

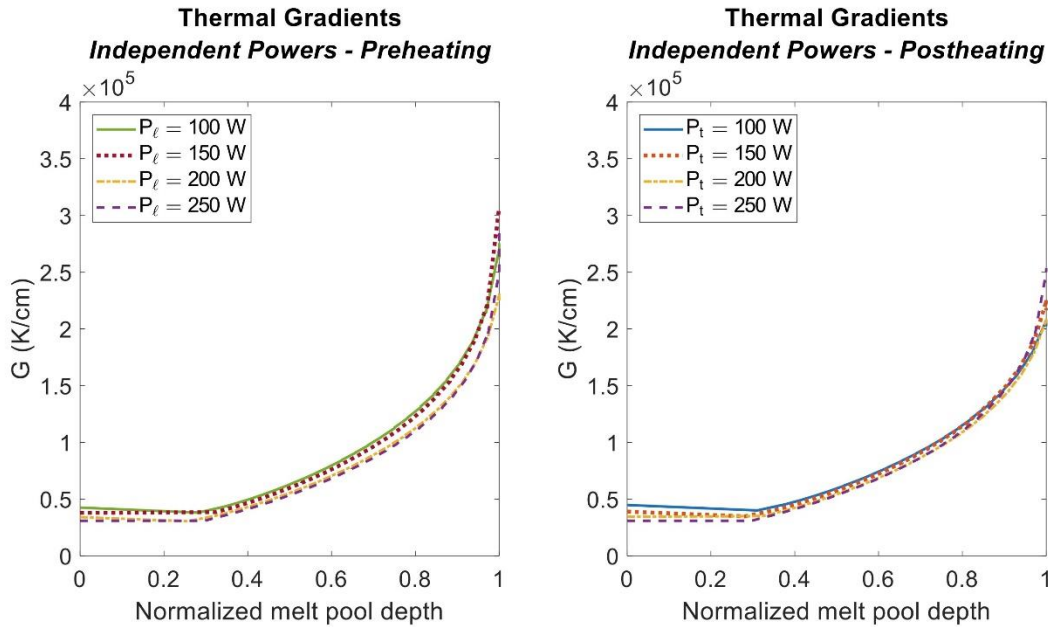


Fig. 11 Thermal gradient vs. normalized melt pool depth for both preheating and post-heating multi-beam scan strategies

The solidification maps for both preheating and post-heating are shown in Fig. 12. These solidification maps show that the simulations modeled here result in mixed grains that transition to columnar grains, which is true for both the preheating and post-heating simulations. As a result, the variation of the individual laser powers provides a negligible influence on the grain morphology. Here, an increase in power is shown to shift the points slightly down and to the left, although these variations are not enough to make any difference in the grain morphology.

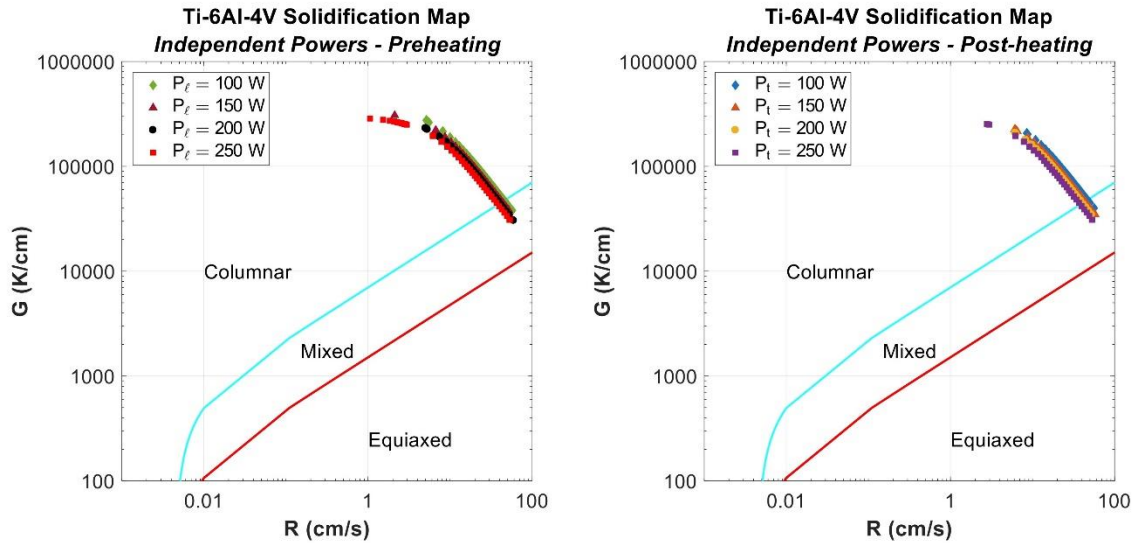


Fig. 12 Solidification maps for both preheating and post-heating multi-beam LPBF

3.3 Identical Beams with Y-Direction Offset

The results displayed in Fig. 13 show both the side and front profiles of the melt pools for scan strategies with four varying offset distances: 50 μm , 100 μm , 150 μm , and 200 μm . The side profiles were all obtained on the $y = 0$ plane to capture the values for the maximum melt pool depth, and the front profiles were obtained on the planes that correspond to the maximum melt pool depth. In these simulations, the lasers remain at a constant power of 300 W with a constant speed of 750 mm/s and an absorption coefficient of 0.35. The maximum melt pool depths, lengths, and widths for the above simulations are summarized in Table 5. Here, an increase in the offset distance causes a decrease in the melt pool length, width, and depth.

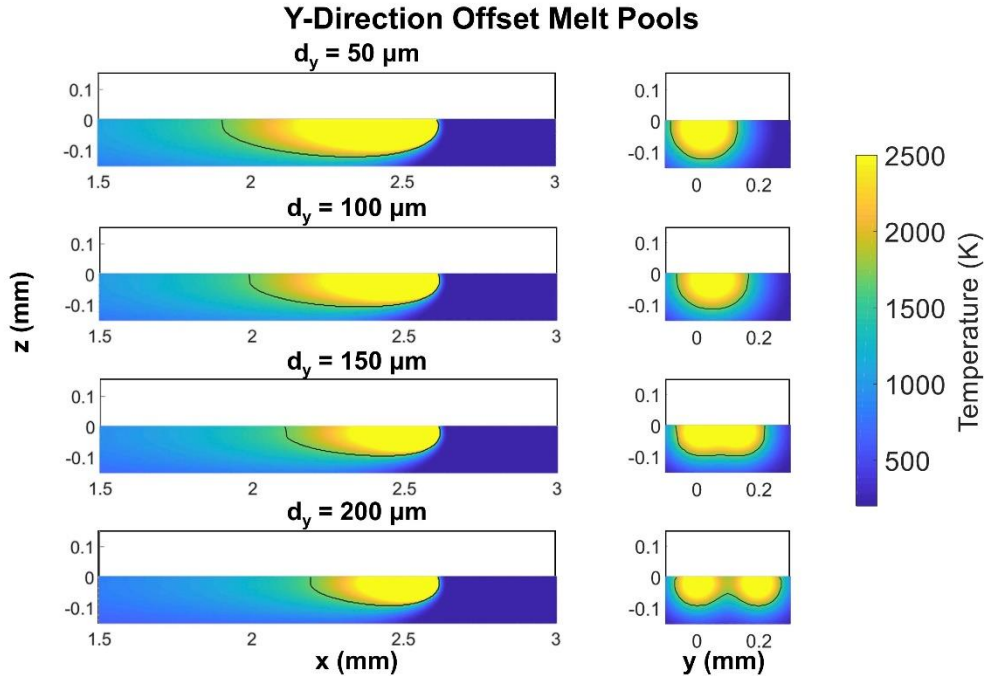


Fig. 13 Melt pool results for multi-beam LPBF with the laser offset in the y-direction

	<i>Maximum Melt Pool Depth (μm)</i>	<i>Melt Pool Length (μm)</i>	<i>Melt Pool Width (μm)</i>
$d = 50 \mu\text{m}$	121.9	712.8	215.6
$d = 100 \mu\text{m}$	106.3	625.0	231.3
$d = 150 \mu\text{m}$	96.9	509.4	287.5
$d = 200 \mu\text{m}$	93.8	421.9	343.8

Table 5 Melt pool dimensions for multi-beam LPBF with offsets in the y-direction

Fig. 14 shows the cooling rates versus the normalized melt pool depth for the y-direction offset multi-beam scan strategies. Here, increasing the offset distance causes an increase in the cooling rate. This result is similar to the conclusion drawn from the x-direction offset. However, Fig. 15 shows the thermal gradient versus the normalized melt pool depth for the simulations with the offset distance in the y-direction. Here, the thermal gradients behave dissimilarly to the x-direction offset; here, there is no clear trend to connect the offset distance to the thermal gradient. In addition, the thermal gradient behaves differently at the top of the melt pool versus the bottom of the melt pool. This may be due to another factor, such as the changing width of the melt pool; however, more research will need to be done to determine the cause of this.

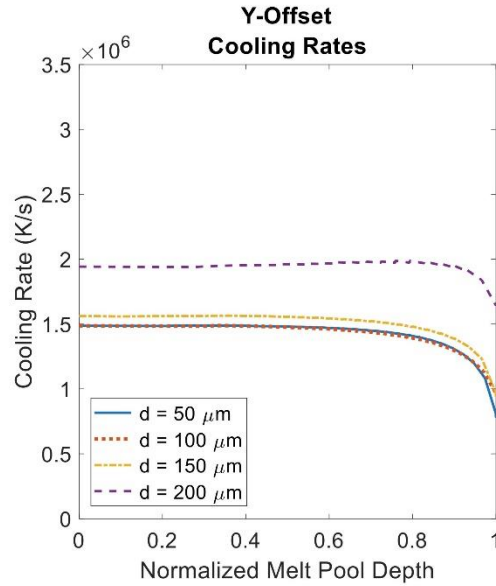


Fig. 14 Cooling rate vs. normalized melt pool depth for multi-beam LPBF with offset distance in the y-direction

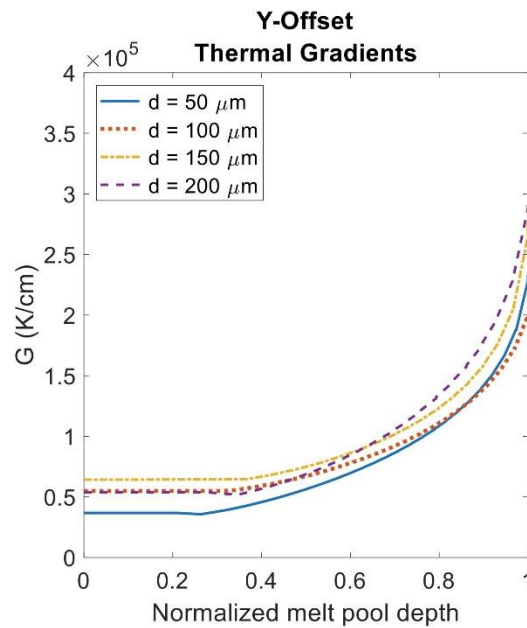


Fig. 15 Thermal gradient vs. normalized melt pool depth for multi-beam LPBF with offset distance in the y-direction

The solidification map for the y-direction simulations, shown in Fig. 16, shows that all of the distances modeled here result in mixed grains that transition to columnar grains with increasing melt pool depth. Additionally, the plots show that an increase in d causes the points to shift slightly above and to the right. This is similar to the conclusions drawn from the simulations with the x-direction offset.

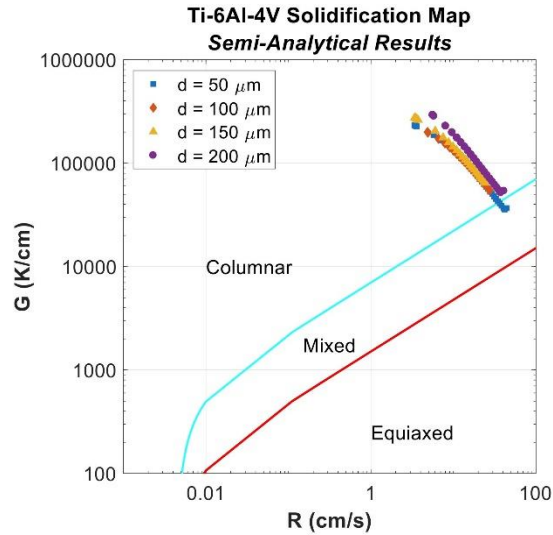


Fig. 16 Solidification map for multi-beam LPBF with offset distance in the y-direction

4 Conclusions

As shown by the multi-beam simulations with the x -direction offset, the addition of a second heat source causes significant changes in the melt pool, which are highly dependent on the distance between the laser beams. The addition of a second heat source causes a longer melt pool with a deeper depth, which transitions to multiple, discrete melt pools as the lasers are spread farther apart. The addition of a second heat source also causes variations in the cooling rate; that is, the cooling rate decreases with the addition of the second heat source, and it approaches the single-beam solution as the lasers spread farther apart. The multi-beam LPBF process also affects the thermal gradients, although these effects are negligible for small distances between lasers (<1 mm). However, the addition of a second beam in the x -direction has been shown to provide a negligible influence in the grain morphology because the results remain in the same morphology regions in the solidification map, regardless of the distance between the multiple beams.

The preheating and post-heating processes resulted in differences in melt pool geometries, which is evident by looking at the dimensions and shapes of the resulting melt pools. In general, the preheating simulations provided slightly longer and deeper melt pools than the post-heating simulations. Additionally, the thermal conditions seen in both preheating and post-heating were very similar to one another; however, the thermal gradients shown in the post-heating simulations were slightly lower than the thermal gradients due to preheating. When plotted on a solidification map, these differences were not enough to alter the microstructure; however, a decrease in the thermal gradient provides the possibility of reducing the residual stresses in the material.

The y -direction offset was also shown to provide variations in the melt pool dimensions. As the distance between the lasers was increased, the melt pool width increased, while both the length and depth decreased. Additionally, an increase in the offset distance caused an increase in cooling rate, which indicates that an increase in offset distance causes a decrease in grain size. Along with this, the thermal gradient was found to have no direct relationship to the offset distance in the y -direction. The exact reason for this is unknown; therefore, more investigation will need to be done to determine the cause of this. In addition, these results all predict the same morphology

regions regardless of the distance between the heat sources. As a result, the results of the y -direction offset show the same general trends as the x -direction simulations.

Due to the scarcity of coordinated multi-beam LPBF machines, it is currently infeasible to experimentally validate the simulations provided in this study. However, the single-beam Rosenthal and semi-analytical solutions have been verified in previous research efforts. It is expected that the superposition of heat sources used in this study are also valid. However, future experimental efforts should be conducted to further validate the results found in this research.

5 Declarations

Funding

This work is funded by the Ohio Space Grant Consortium Fellowship.

Conflicts of interest

All authors declare that they do not have any potential conflicts of interest.

Ethics approval

Not applicable.

Consent to participate

Not applicable.

Consent for publication

Not applicable.

6 References

- [1] Grasso M, Colosimo BM (2017) Process defects and in situ monitoring methods in metal powder bed fusion: A review. *Meas Sci Technol* 28. <https://doi.org/10.1088/1361-6501/aa5c4f>.
- [2] Kobryn PA, Semiatin SL (2001) The laser additive manufacture of Ti-6Al-4V. *JOM* 53:40–2. <https://doi.org/10.1007/s11837-001-0068-x>.
- [3] Li F, Wang Z, Zeng X (2017) Efficient fabrication of Ti6Al4V alloy by means of multi-laser beam selective laser melting. *Solid Free. Fabr. Proc.*, Austin.
- [4] Masoomi M, Thompson SM, Shamsaei N (2017) Quality part production via multi-laser additive manufacturing. *Manuf Lett* 13:15–20. <https://doi.org/10.1016/j.mfglet.2017.05.003>.
- [5] Heeling T, Wegener K (2016) Computational investigation of synchronized multibeam strategies for the selective laser melting process. *Phys Procedia* 83:899–908. <https://doi.org/10.1016/j.phpro.2016.08.094>.
- [6] Heeling T, Wegener K (2018) The effect of multi-beam strategies on selective laser melting of stainless steel 316L. *Addit Manuf* 22:334–42. <https://doi.org/10.1016/j.addma.2018.05.026>.
- [7] Abe F, Osakada K, Shiomi M, Uematsu K, Matsumoto M (2001) The manufacturing of hard tools from metallic powders by selective laser melting. *J Mater Process Technol* 111:210–3. [https://doi.org/10.1016/S0924-0136\(01\)00522-2](https://doi.org/10.1016/S0924-0136(01)00522-2).
- [8] Aggarangsi P, Beuth JL (2006) Localized preheating approaches for reducing residual stress in additive manufacturing. *Solid Free. Fabr. Proc.*, Austin.

- [9] Rosenthal D (1946) The Theory of Moving Source of Heat and its Application to Metal Transfer. ASME Trans 43:849–66.
- [10] Gockel J, Klingbeil N, Bontha S (2016) A Closed-Form Solution for the Effect of Free Edges on Melt Pool Geometry and Solidification Microstructure in Additive Manufacturing of Thin-Wall Geometries. Metall Mater Trans B 47:1400–8. <https://doi.org/10.1007/s11663-015-0547-z>.
- [11] Vasinota A, Beuth JL, Ong R (2001) Melt Pool Size Control in Thin-Walled and Bulky Parts via Process Maps. Solid Free. Fabr. Proc., Austin.
- [12] Bontha S, Klingbeil NW (2003) Thermal process maps for controlling microstructure in laser-based solid freeform fabrication. Solid Free. Fabr. Proc., Austin.
- [13] Bontha S, Klingbeil NW, Kobryn PA, Fraser HL (2009) Effects of process variables and size-scale on solidification microstructure in beam-based fabrication of bulky 3-D structures. Mater Sci Eng A 513–514:311–8. <https://doi.org/10.1016/j.msea.2009.02.019>.
- [14] Plotkowski A, Kirka MM, Babu SS (2017) Verification and validation of a rapid heat transfer calculation methodology for transient melt pool solidification conditions in powder bed metal additive manufacturing. Addit Manuf 18:256–68. <https://doi.org/10.1016/j.addma.2017.10.017>.
- [15] Carslaw H, Jaeger J (1959) The Use of Sources and Sinks in Cases of Variable Temperature. Conduction of Heat in Solids. 2nd ed., Oxford: Oxford University Press; p. 255–60.
- [16] Hou ZB, Komanduri R (1998) Magnetic field assisted finishing of ceramics-part I: Thermal Model. J Tribol 120:645–51. <https://doi.org/10.1115/1.2833761>.
- [17] Komanduri R, Hou ZB (2000) Thermal analysis of the arc welding process: Part I. General solutions. Metall Mater Trans B 31:1353–70. <https://doi.org/10.1007/s11663-000-0022-2>.
- [18] Komanduri R, Hou ZB (2001) Thermal analysis of the laser surface transformation hardening process. Int J Heat Mass Transf 44:2845–62. [https://doi.org/10.1016/S0017-9310\(00\)00316-1](https://doi.org/10.1016/S0017-9310(00)00316-1).
- [19] Stump B, Plotkowski A (2019) An adaptive integration scheme for heat conduction in additive manufacturing. Appl Math Model 75:787–805. <https://doi.org/10.1016/j.apm.2019.07.008>.
- [20] Evans R, Walker J, Middendorf J, Gockel J (2020) Modeling and Monitoring of the Effect of Scan Strategy on Microstructure in Additive Manufacturing. Metall Mater Trans A <https://doi.org/10.1007/s11661-020-05830-0>.

Figures

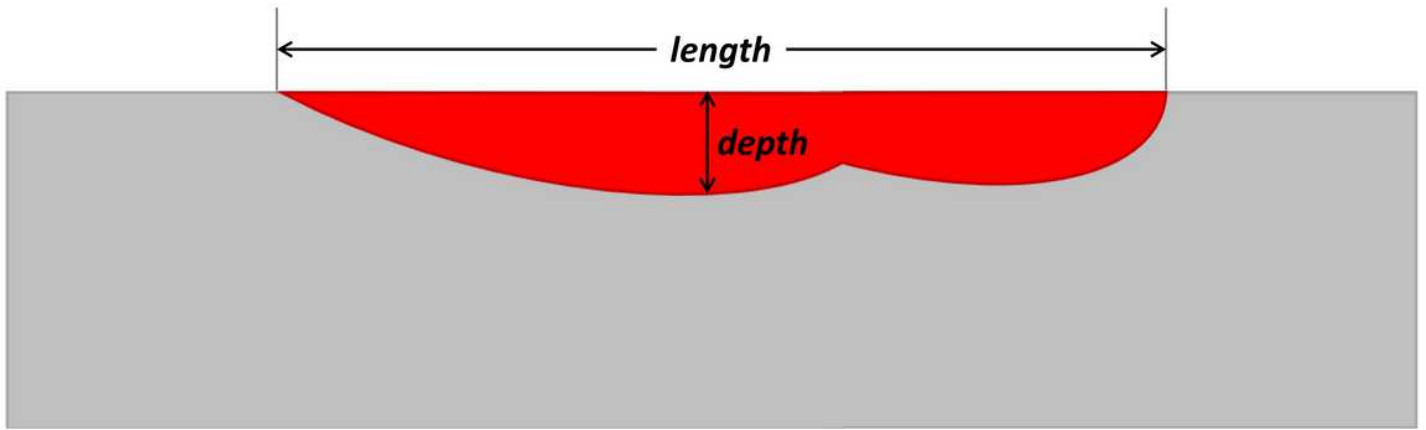


Figure 1

Melt pool dimensions for multi-beam LPBF

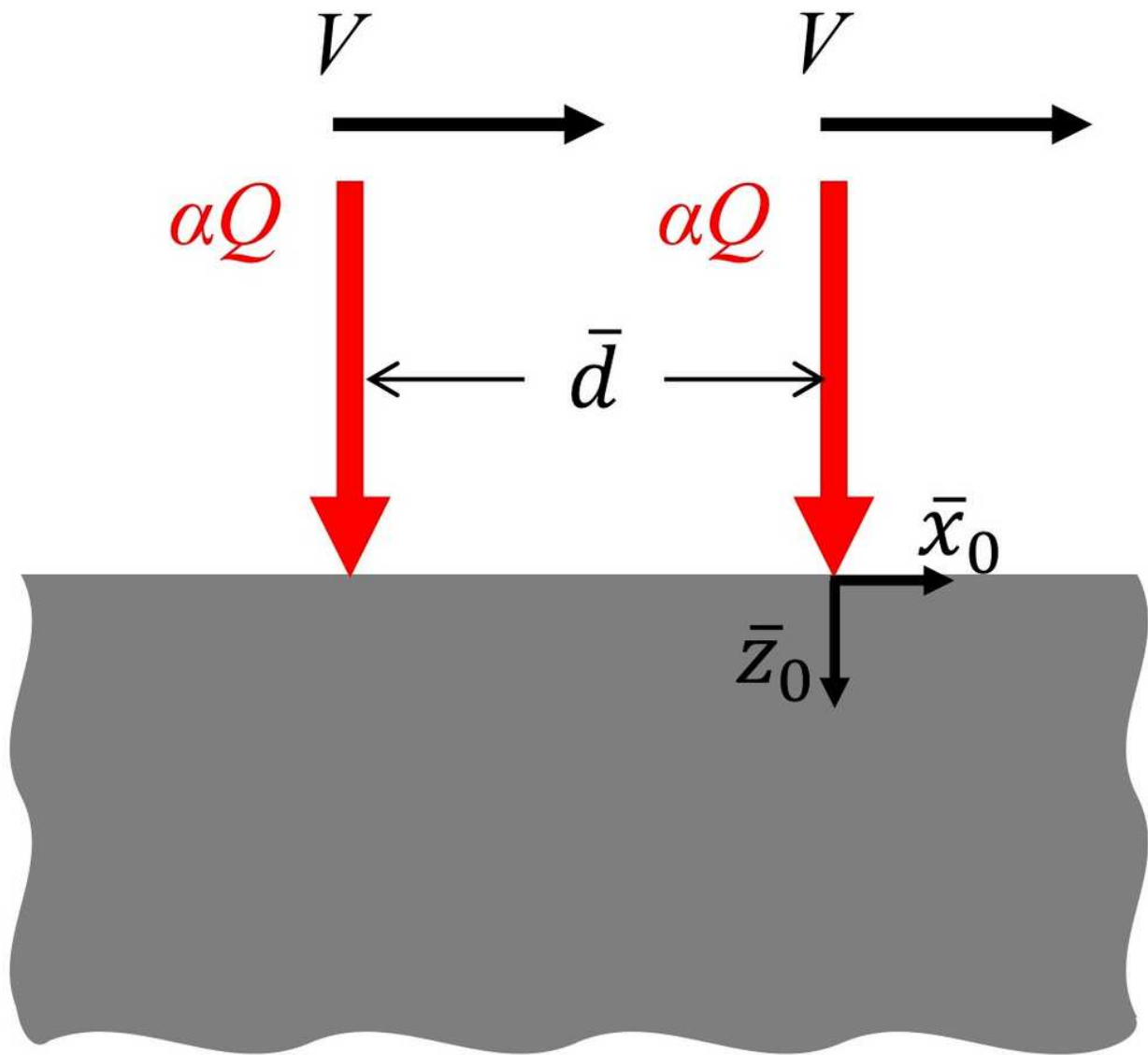


Figure 2

The coordinated multi-beam LPBF configuration that is modeled by the Rosenthal solution

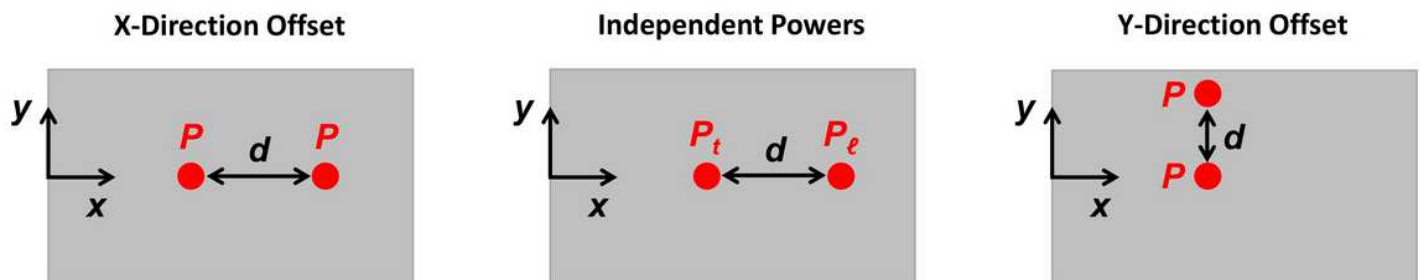


Figure 3

The scanning strategies that are modeled by the multi-beam semi-analytical model

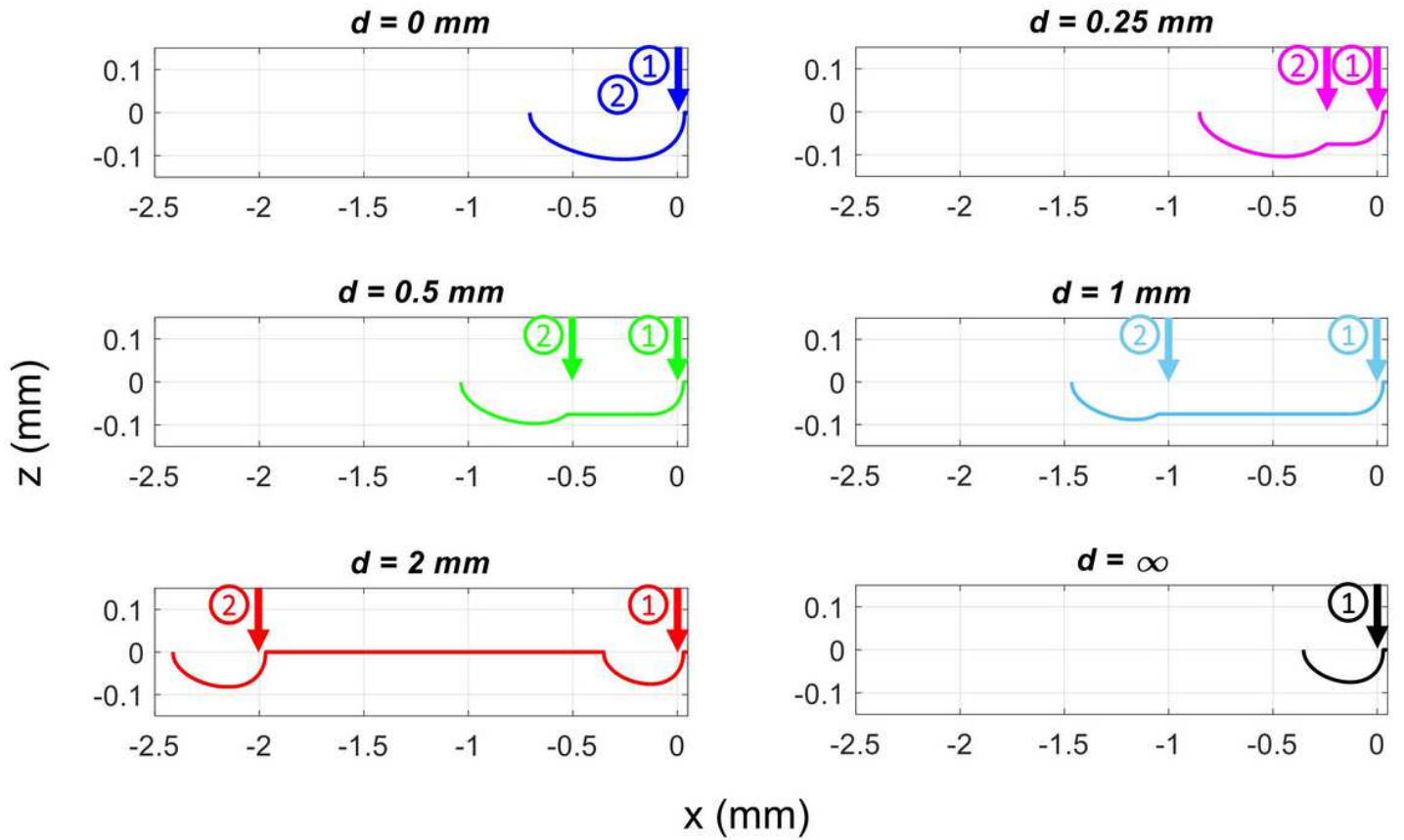


Figure 4

Melt pool geometries of multi-beam LPPF, as predicted by the Rosenthal solution

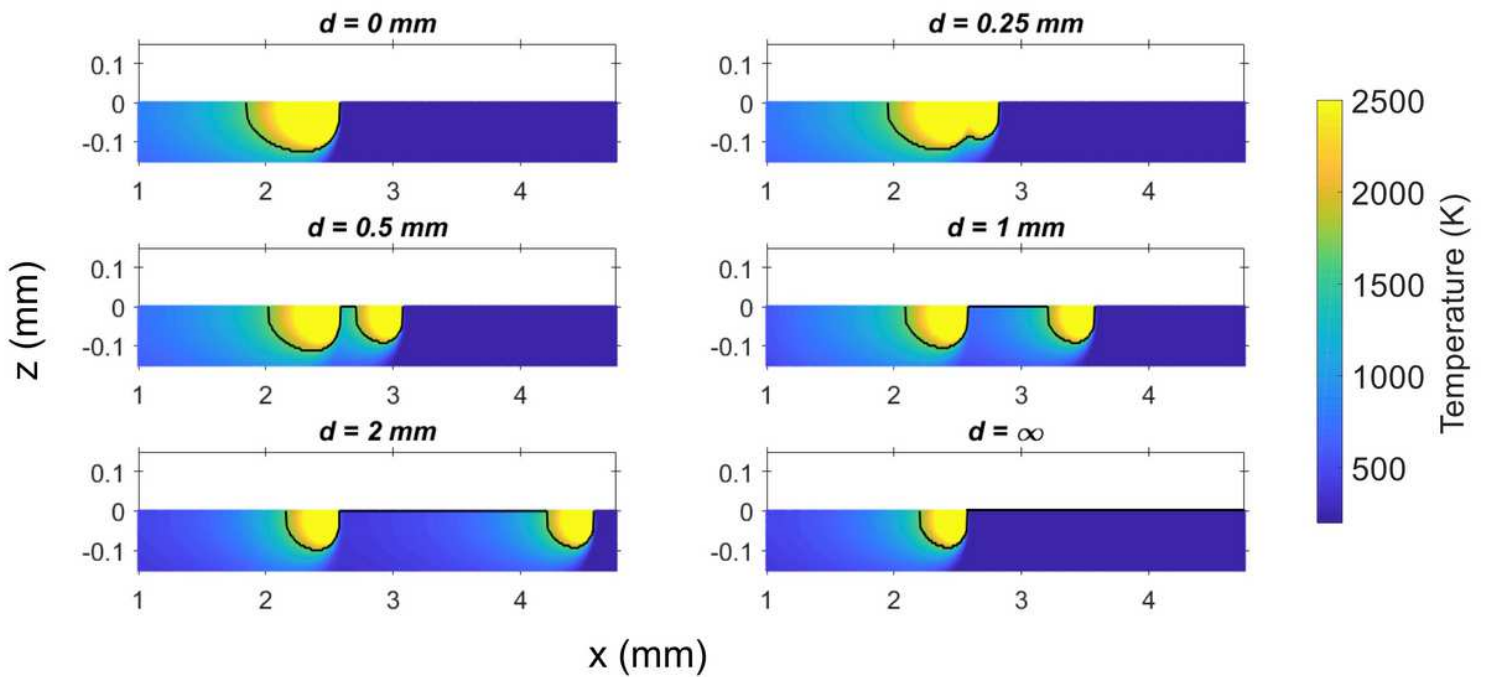


Figure 5

Melt pool geometries of multi-beam LPBF, as predicted by the semi-analytical model

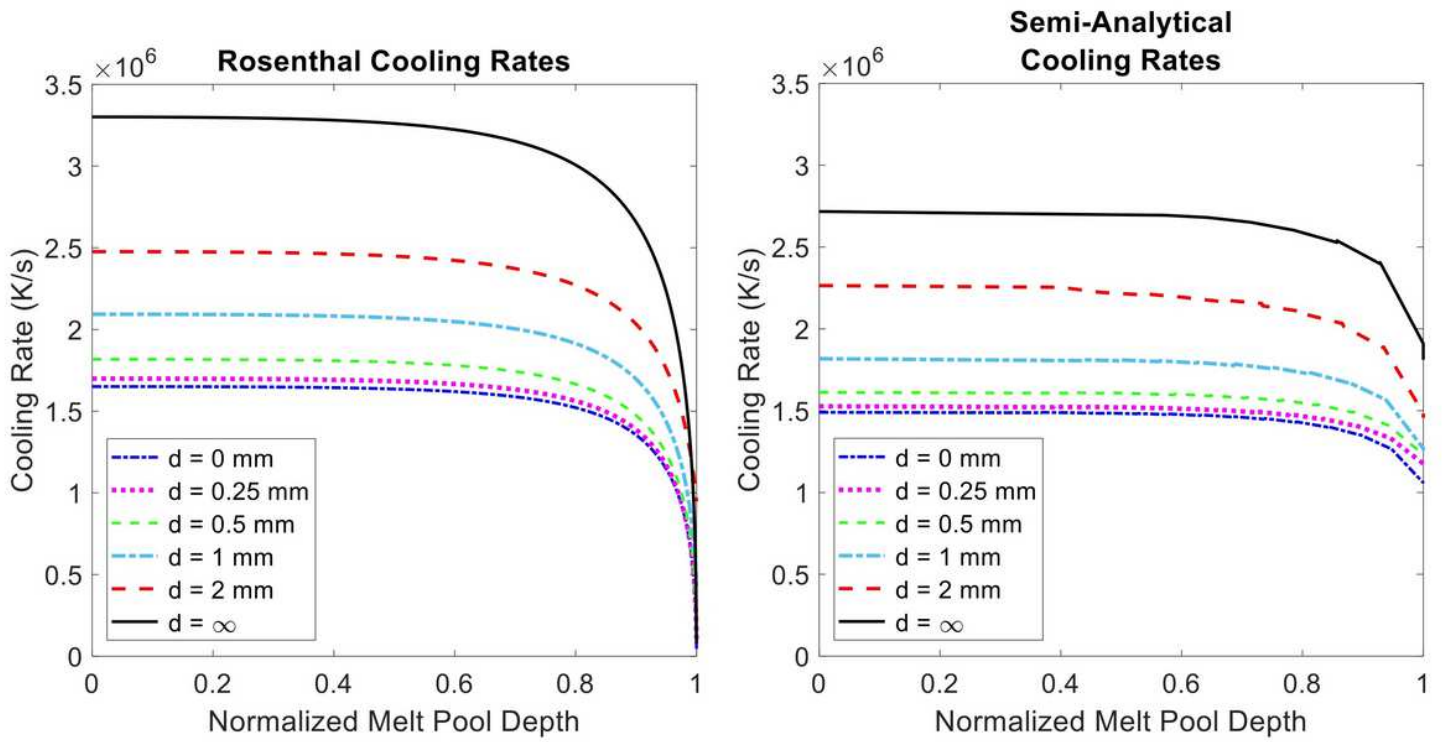


Figure 6

Cooling rate vs. normalized melt pool depth in multi-beam LPBF with x-direction beam offset. These results were obtained with both the Rosenthal solution (left) and the semi-analytical solution (right)

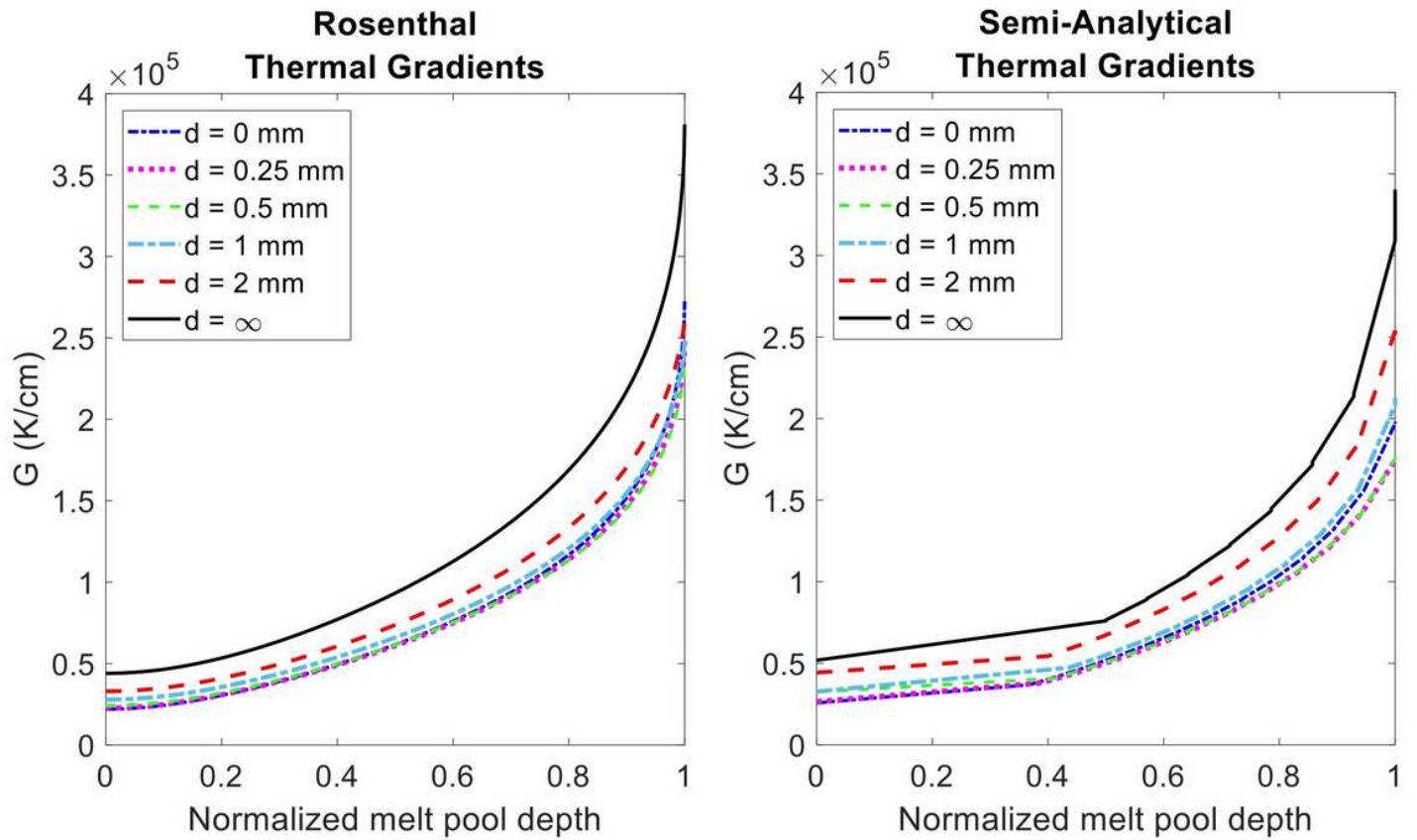


Figure 7

Thermal gradient vs. normalized melt pool depth in multi-beam LPBF with x-direction beam offset. These results were obtained with both the Rosenthal solution (left) and the semi-analytical solution (right)

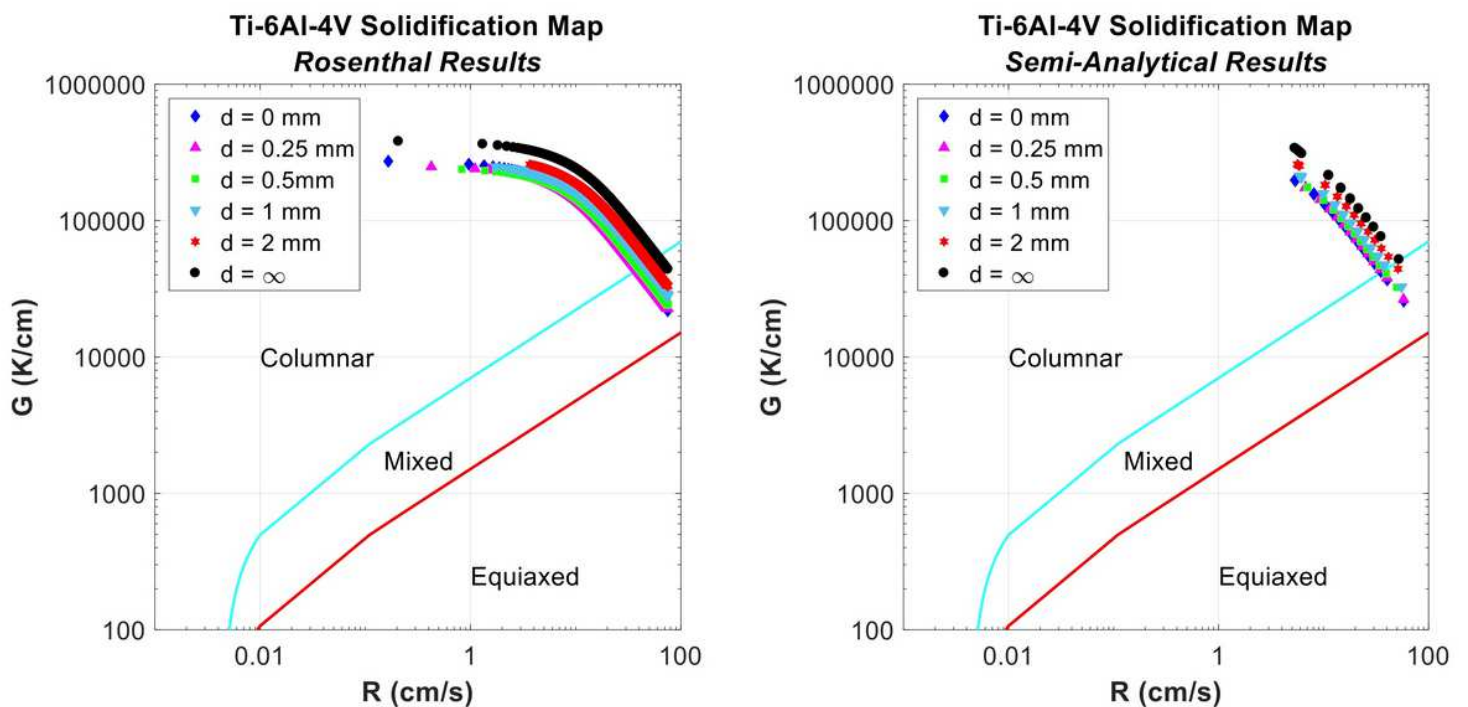


Figure 8

Solidification maps for multi-beam LPBF, using both the Rosenthal (left) and semi-analytical (right) approaches

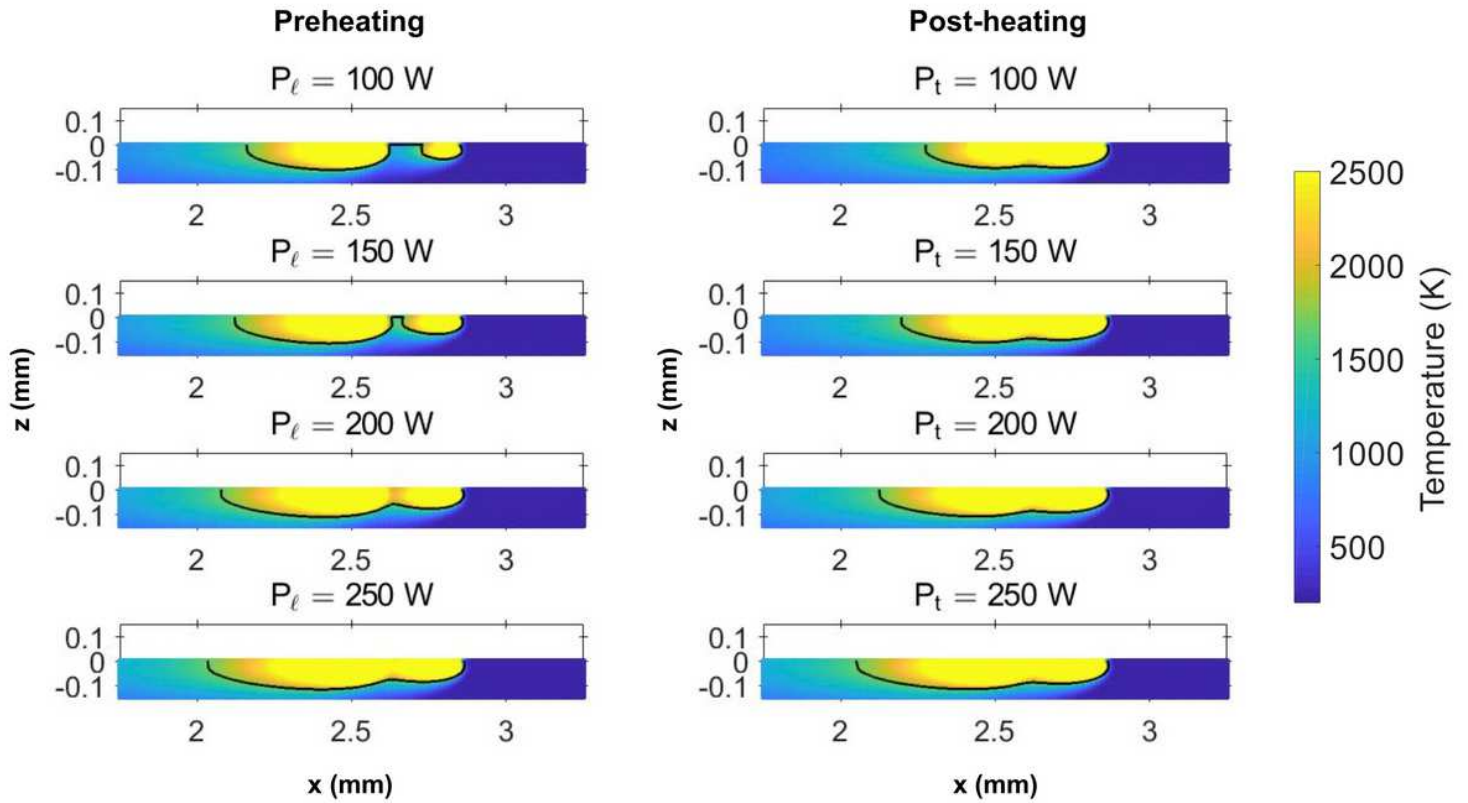


Figure 9

Melt pool results for preheating and post-heating multi-beam LPBF

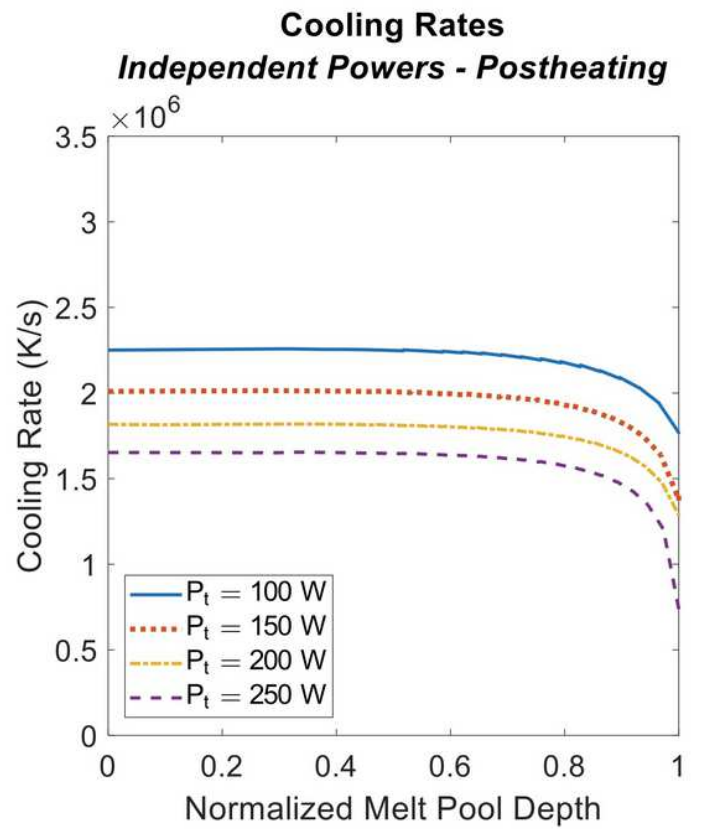
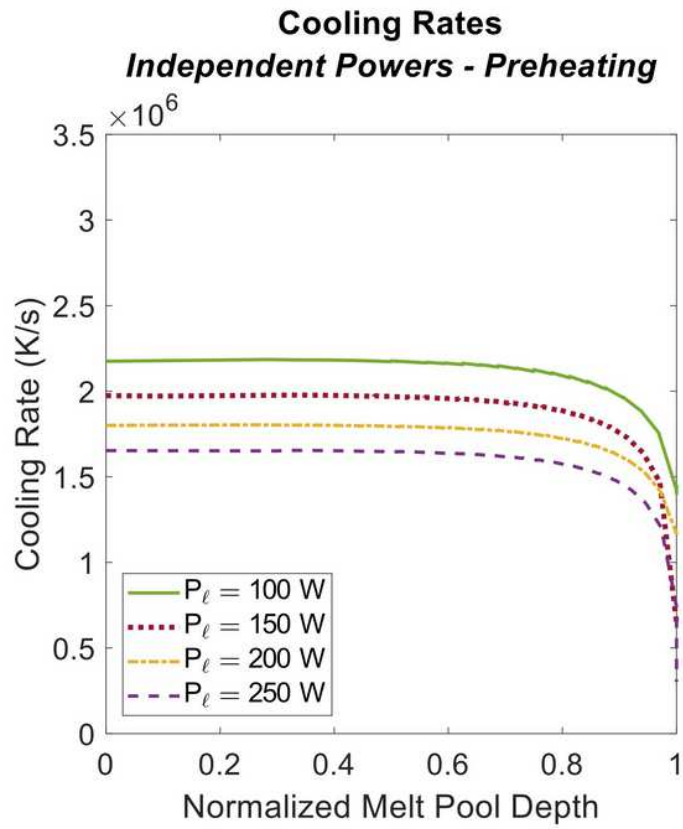


Figure 10

Cooling rate vs. normalized melt pool depth for both preheating and post-heating multi-beam scan strategies

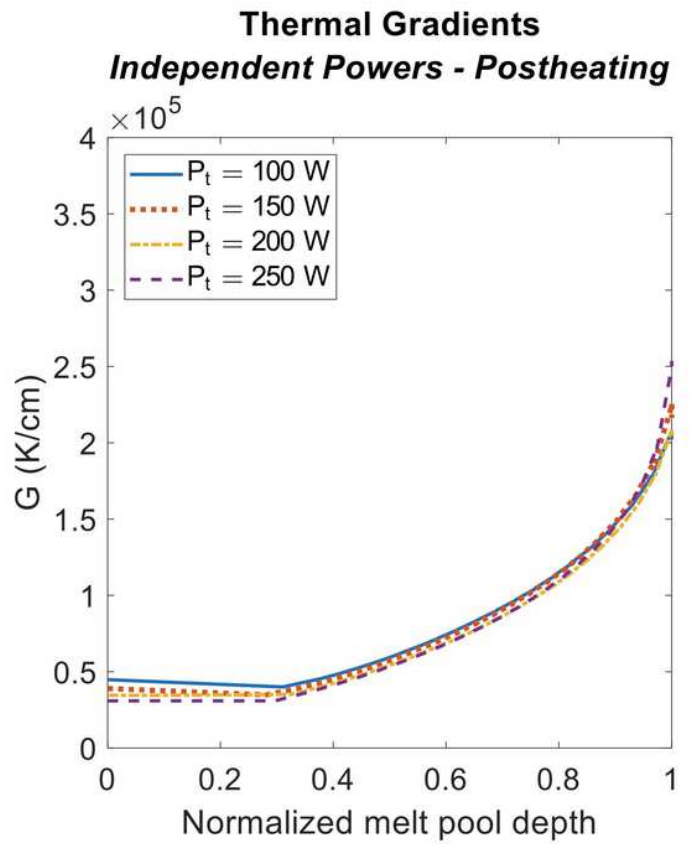
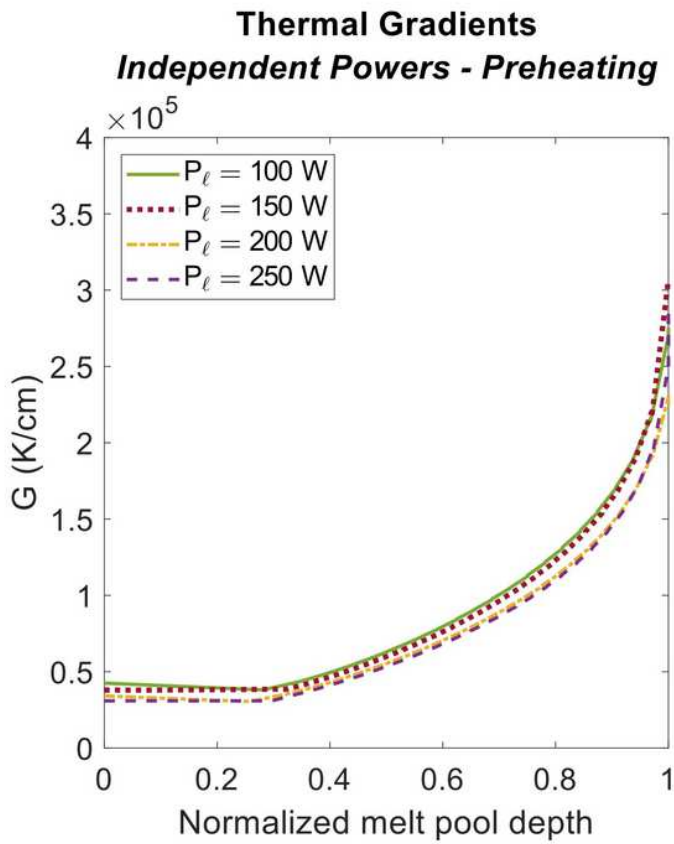


Figure 11

Thermal gradient vs. normalized melt pool depth for both preheating and post-heating multi-beam scan strategies

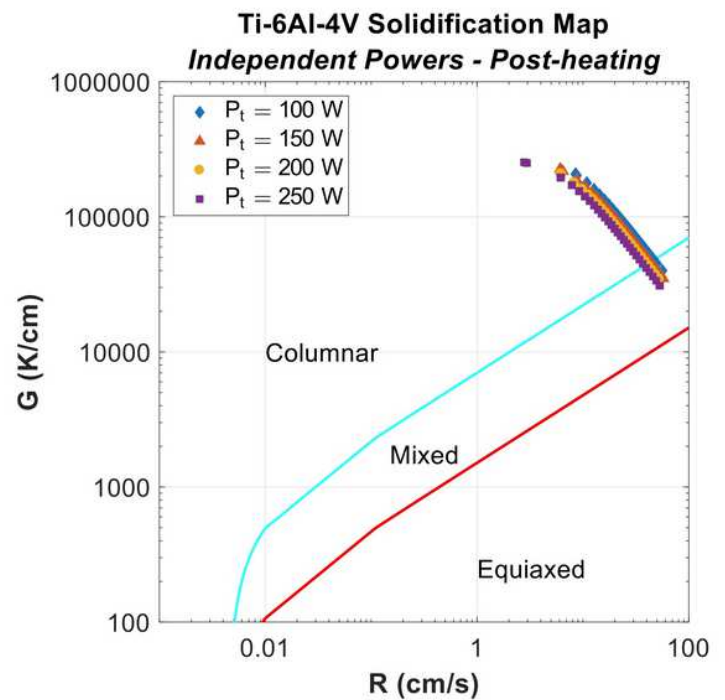
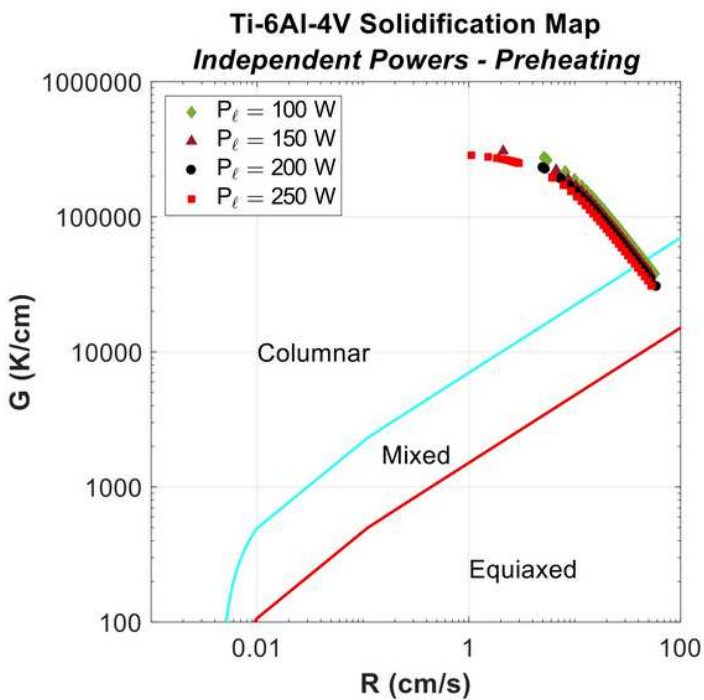


Figure 12

Solidification maps for both preheating and post-heating multi-beam LPBF

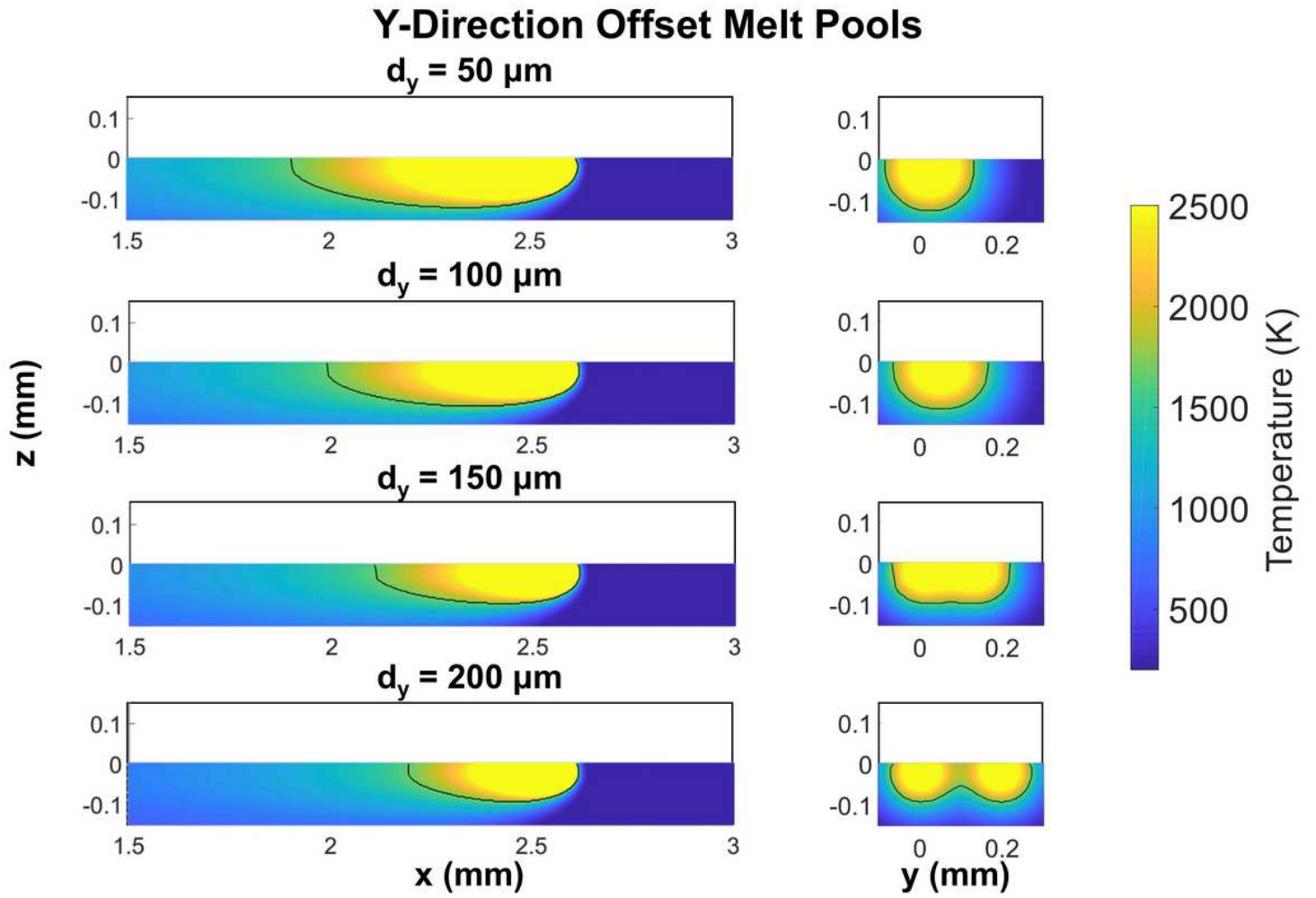


Figure 13

Melt pool results for multi-beam LPBF with the laser offset in the y-direction

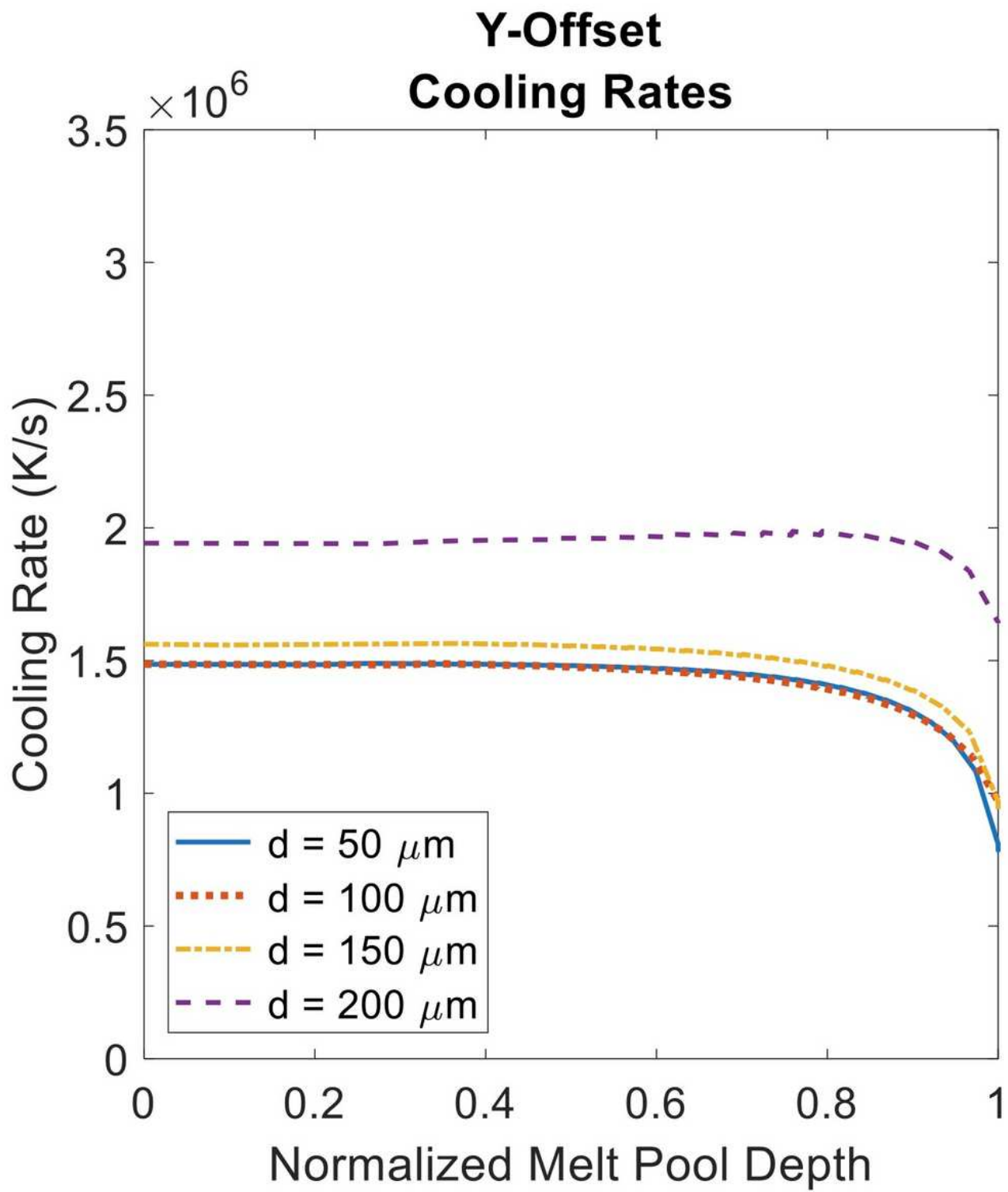


Figure 14

Cooling rate vs. normalized melt pool depth for multi-beam LPBF with offset distance in the y-direction

Y-Offset

Thermal Gradients

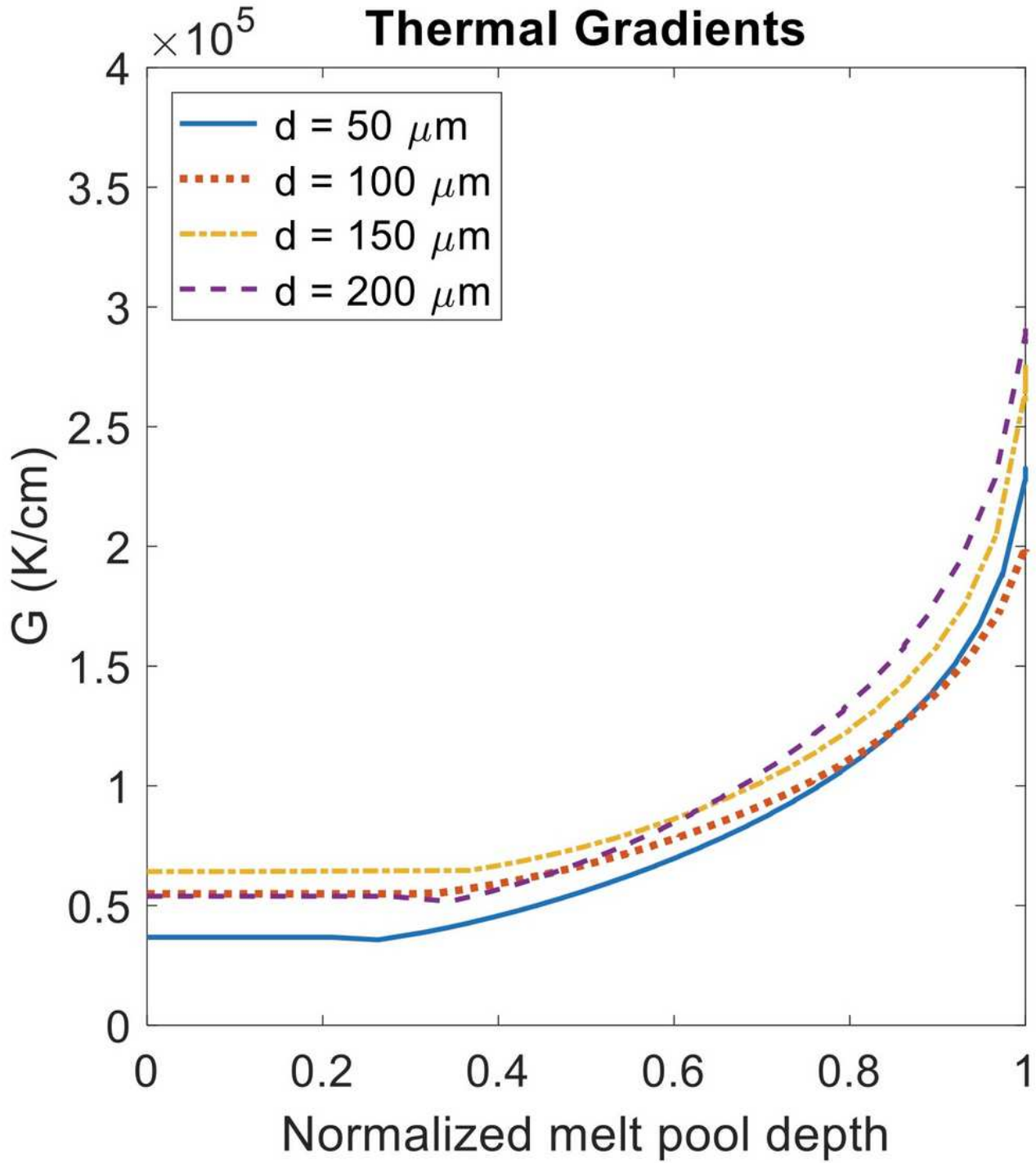


Figure 15

Thermal gradient vs. normalized melt pool depth for multi-beam LPBF with offset distance in the y-direction

Ti-6Al-4V Solidification Map

Semi-Analytical Results

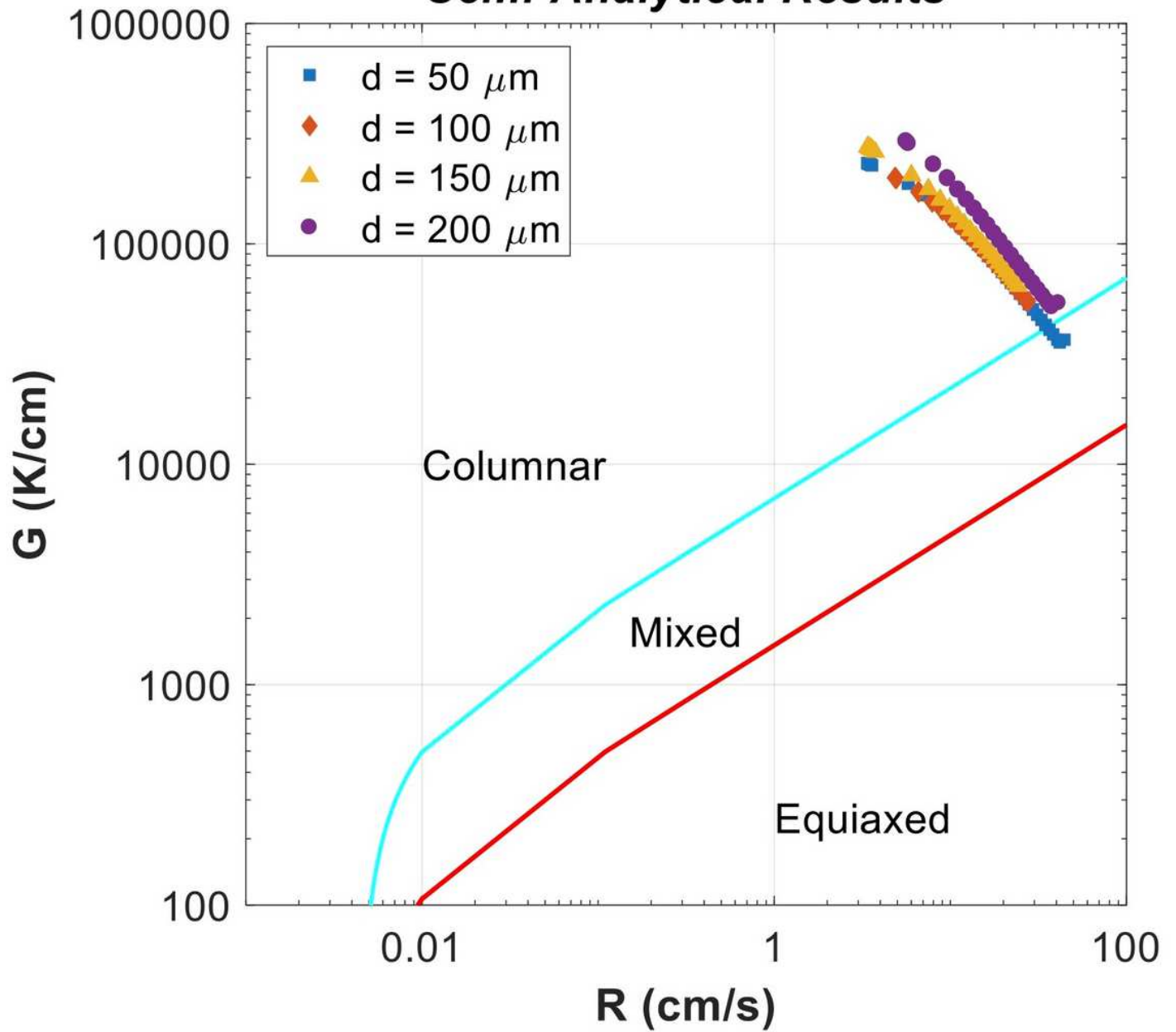


Figure 16

Solidification map for multi-beam LPBF with offset distance in the y-direction